An Analysis of the Forgeability of Ti-10V-2Fe-3Al β Titanium alloy using a combined EM+Avrami Material Constitutive Model

Paul M. Souza, Giribaskar Sivaswamy*, Liza Hall and Salaheddin Rahimi

Advanced Forming Research Centre, National Manufacturing Institute Scotland, University of Strathclyde, 85 Inchinnan Drive, Inchinnan, Renfrewshire, PA4 9LJ, United Kingdom

*Corresponding author
E mail: giribaskar.sivaswamy@strath.ac.uk
Phone: +44-141-5345258

Highlights

- The Ti-10V-2Fe-3Al alloy with an initial lamellar microstructure exhibited flow softening due to the globularisation of fragmented primary α lamellae within the β matrix.
- Dynamic recrystallisation of β grains and stress induced morphological changes to lamellar α phase resulted in steady state flow.
- A new constitutive material model (Estrin Mecking +Avrami) with minimal material constants was developed with more than 95% convergence.
- The constitutive model implemented into a finite element modelling package revealed good predictive capability for open-die sub-transus forging of Ti-10V-2Fe-3Al alloy.

Graphical abstract

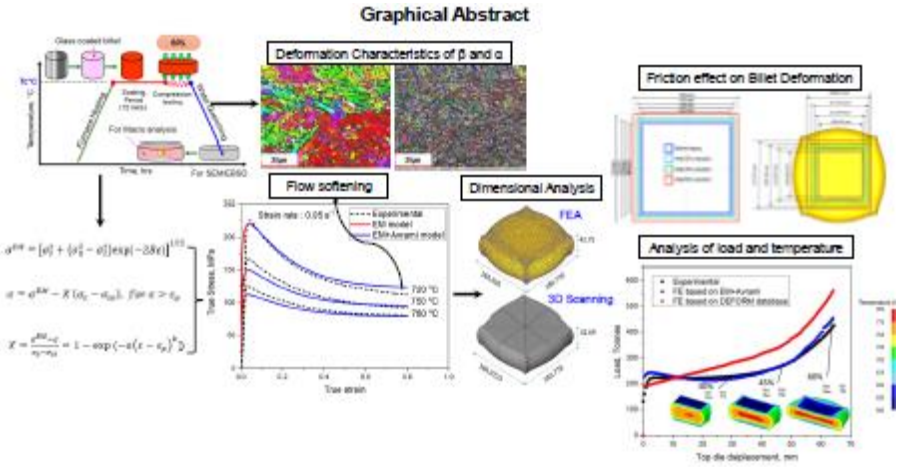

Abstract:

A constitutive model was developed to predict the high temperature sub-transus flow behaviour of a metastable β Ti-10V-2Fe-3Al alloy, and its applicability for industrial scale forging process has been evaluated using a finite element simulation. Cylindrical samples extracted from a cogged billet of the alloy after β recrystallisation treatment were subjected to hot compression tests at sub-transus temperatures ranging from 720°C to 780°C with an increment of 15 °C under varying strain rates from 0.025 to 0.2 s^{-1}. The sub-transus flow curves of the alloy exhibited work hardening followed by dynamic recovery and flow softening beyond the strain equivalent to peak stress. Formation of low angle grain boundaries within the prior β grains and dynamic recrystallisation of β phase were observed to contribute to the flow softening. A constitutive model based on Estrin Mecking and Avrami methods was developed with minimised number of material constants, using the data derived from the hot compression tests. The model was successfully verified using the deformation behaviour measured for the alloy in the region of interest. The constitutive model was implemented into a finite element package as a user subroutine to predict the flow behaviour in industrial scale billets during open die hot forging processes and validated using experimental trials. A fairly good predictive capability with more than 95% convergence for open die forging was achieved, confirming the suitability of the material model developed for predicting sub-transus forgeability of the Ti-10V-2Fe-3Al alloy during industrial scale forging.

Keywords: Titanium alloys, Constitutive modeling, FE simulation, Open-die forging, Dynamic recrystallisation, EBSD

1.0 Introduction

An abundance of different microstructures makes β-Titanium alloys attractive as compared to classic α+β alloys in the aerospace industry for manufacturing structural components. High strength to density ratio, excellent hardenability, hot formability, good fatigue resistance are the main attractive characteristics of these alloys. The Ti-10V-2Fe-3Al is one of the metastable β titanium alloys developed for manufacturing critical components like landing gears in aerospace industry by hot forging [1]. A relatively low β-transus temperature (~795±5 °C) of Ti-10V-2Fe-3Al alloy, compared to those of α+β alloys such as Ti-6Al-4V (~995±5 °C), allows manufacturing of near net shape parts by forging at comparatively low temperatures using low cost tools and dies. However, the hot isothermal forging technique is generally adopted to obtain near net shape aerospace components from metastable β-Titanium alloys like Ti-10V-2Fe-3Al due to its narrow working range below the β transus [2]. Further, critical forging cycles such as the low temperature finish forging at sub-transus temperatures were adopted to enhances the globularisation of α and β phases, which lead to better combination of strength and ductility [3]. Therefore, a better understanding on the influence of strain, strain rate and temperature during hot working is needed. This necessitates the requirement for highly accurate predictive models to be used during industrial forging.

The flow stress, strain rate and deformation temperature have generally been related to one another via constitutive descriptions. Various material constitutive descriptions used in finite element (FE) tools are the fundamental step to foresee the deformation behaviour. These constitutive models are divided into empirical models and physical based models [4]. The empirical based models are a mathematical relationship with no significant physical meaning. These empirical descriptions are established based on experimental data and extrapolated to fit various process conditions [5]. On the other hand, physical based models consider the physical significance of the material behaviour with respect to process parameters during deformation [6]. The accuracy in predicting the deformation behaviour using the FE based models mainly depends on the predictability of the implemented material models [7].

Many investigations on developing constitutive models for metals and alloys are reported [4]. However, the studies mainly focused on metastable α+β alloys, such as Ti-6Al-4V, and

less attention has been given to metastable β titanium alloys [8, 9]. A physically based model developed by Bobbili et al., [10] to predict deformation behaviour of Ti-10V-2Fe-3Al alloy, taking into consideration of work hardening and dynamic recovery, provides a very good estimation of the flow behaviour in the β phase region. A modified Johnson-Cook (J-C) constitutive model for flow behaviour prediction in Ti-10V-2Fe-3Al alloy for high temperature and high strain rate deformation was proposed by Buzaud et al., [11]. However, the model predicts the flow behaviour only during the initial work hardening stage of the alloy. A comparison of J-C model and modified Zerilli-Armstrong model developed for Ti-6Cr-5Mo-5V-4Al, β titanium alloy provided an accurate prediction of deformation behaviour over high strain rate ranges, although, it failed to predict the work hardening behaviour of the alloy [12]. Among the various reported constitutive models for α+β titanium alloys, a combined Estrin-Mecking and Avrami (EM+Avrami) model is reported to be capable of predicting the flow behaviour in Ti-6Al-4V alloy considering the work hardening and flow softening [13]. Therefore, a constitutive model that can predict the deformation behaviour in Ti-10V-2Fe-3Al alloy, considering the mechanisms related to deformation and microstructural evolution, is needed for the increasing industrial demands.

The major objective of this work is to understand the deformation behaviour of the metastable Ti-10V-2Fe-3Al alloy at sub-transus working temperatures, and to develop a suitable constitutive material model to predict the flow behaviour. The EM+Avrami constitutive model has been identified as a potential approach for accurate predictions of the flow behaviour. Considering the application of the developed model in industrial scale, it has been incorporated into an FE based package to predict flow behaviour during bulk metal forging and the results are reported.

2.0 Material and experimental procedures

The as-received material used in this study was taken from cogged cylindrical billets of 280 mm diameter of TIEMTAL® 10-2-3 (Ti-10V-2Fe-3Al) alloy supplied by TIMET Savoie. The nominal chemical composition of the alloy is provided in Table 1. The β-transus temperature of the same grade of material with similar chemical compositions were reported to be in the range of ~795±5 °C [14]. The as-received material was subjected to β recrystallisation treatment at 950 °C for 2 hrs in a vacuum furnace, and furnace cooled to room temperature with an average cooling rate of ~5 °C/min. Cylindrical samples with 12

mm diameter and 18 mm height were extracted from the β recrystallised billets for hot isothermal compression tests with their axes along the length of the as-received billet.

2.1 Hot compression testing

The hot isothermal compression tests were conducted using a screw driven Zwick/Roell Z150 machine equipped with a split furnace at temperatures ranging from 720°C to 780°C with an interval of 15 °C, under varying strain rates including $0.025s^{-1}$, $0.05\ s^{-1}$, $0.075\ s^{-1}$, $0.1\ s^{-1}$ and $0.2\ s^{-1}$. Samples were coated with Bonderite L-FGFB-412 delta glaze to minimise oxidation during hot deformation.

For each test, a sample was loaded into the machine and heated in the attached resistance heating furnace and soaked for 15 minutes at the deformation temperature prior to the start of the test. The sample was then subjected to hot compression to 60%, and immediately removed from the furnace and placed on a refractory material, at about transfer time of less than 5 s, followed by air-cooling to room temperature (Fig. 1a). Thermocouples were attached to the top and bottom platens of the compression testing machine to monitor the uniform temperature of the sample and dies inside the furnace. More thermocouples were used to control the temperatures of the furnace to get the desired test temperature. The tie rods fitted to the top and bottom cross heads of the testing machine were made of Nimonic 80A alloy. Flow curves derived from load- displacement data were corrected for the test frame compliance. The top and bottom platens connected to the tie rods were made from tungsten and coated with boron nitride to act as lubricant between the workpiece and the die (Fig. 1b). In order to understand the microstructure evolution during hot compression, three samples were subjected to compression tests at 750°C and under strain rate of $0.075\ s^{-1}$ to varying deformation levels (i.e., 30%, 45% and 60% reductions) (Fig. 2). These samples were then immediately water quenched (~5 seconds), following the compression tests, to room temperature to minimise the level of meta-dynamic recrystallisation.

2.2 Microstructure characterisation

Microstructure characterisations of the hot compression tested samples were carried out using optical microscopy (OM) and scanning electron microscopy (SEM). For the analyses with OM, the samples were mechanically ground and polished to a mirror finished condition and etched. The etching was carried out in two stages using Krolls reagent in the first stage and 10%HF+90%H_2O in the second stage to reveal grains and grain boundaries.

For the analyses with SEM, the mirror finished samples were electro-polished using Struers's electrolyte A3, which contained 600 ml methanol, 360 ml butoxy-ethanol and 60 ml perchloric acid. A Struers LectroPol-5, automatic electrolytic polishing and etching equipment, was used for electro-polishing. The electro-polishing was done at 10-15°C, under 35 V voltage for 15 s. The electro-polished samples were then characterised using FEI Quanta-650 field-emission gun (FEG) microscope operating at 20 kV. Both the secondary electron (SE) and back scattered electron (BSE) modes were opted during SEM analysis. Additionally, EBSD maps were acquired from the centre of mid-plane at the high strain zone of each tested sample using a fully automated HKL-EBSD system interfaced to the FEG-SEM, with an accelerating voltage of 20 kV and a 100 µm dia. aperture. A minimum of 86% of the scanned areas, each with a typical 70 µm × 50 µm area, were indexed. All the above microstructure characterisations using different techniques were carried out on an axial plane with a normal perpendicular to the compression direction.

2.3 Forging trials

To validate the results of FE simulations, samples of Ti-10V-2Fe-3Al alloy in the form of cube with 105 mm × 105 mm ×105 mm dimensions were extracted from the as-received cylindrical billets (Fig. 3). The as-received cogged cubes were β recrystallised at 950 °C, which is ~150 °C above the β-transus temperature (~795±5 °C) of the alloy. To avoid oxidation, the heat treatment was carried out in a VFE/TAV TPH25/25/35 horizontal vacuum furnace, followed by furnace cooling to room temperature. The orientation of cubes was maintained in a way that the forging direction was parallel to the cogging direction (CD) (i.e., radial axis) of the as-received billets (Fig. 3a and b).

Forging was carried out at 750°C, at sub-transus region, to three levels of reductions in height including 30%, 45% and 60%. A hydraulic press with 500T capacity, fitted with dies capable of heating to 450 °C, was used for the open die forging trials. The temperature of the top and bottom dies during forging was maintained at ~400 °C. The cubes were coated with delta-glaze to minimise oxidation during forging (Fig. 3b). The cubes were loaded into a Carbolite furnace and soaked at 750°C for 2 hrs. The top and bottom dies were lubricated with a synthetic graphite lubricant to reduce friction between the cubes and the die assembly. The forging was carried out in a strain rate-controlled mode where the maximum strain rate did not exceed 0.075 s^{-1}. The forged cubes were transferred to a furnace maintained at 600°C for controlled cooling. The forged cubes were then cooled down to 100 °C under a cooling

rate of 10-12 °C/min using an industrial fan. Finally, the forged cubes were left outside of the furnace and air cooled to the room temperature.

2.4 3D scanning of the forged cubes

Non-contact optical scanning technique using GOM ATOS® was adopted to analyse the shape and dimensional changes of the cubes after three levels of reduction during the forging trials (Fig. 4). This was to compare the results of dimensional changes predicted by the FE using DEFORM ®3D with those of the forging trials after three levels of reduction. The 3D models of the forged cubes were constructed which can be used to determine dimensional changes to ± 5µm accuracy [15].

3.0 Results

3.1. Microstructure of the as-received billet

SEM micrographs recorded from a plane perpendicular to the CD revealed the presence of primary α in the form of lamellar and globular morphologies within prior β grains (Fig. 5). Evidence for the formation of discontinuous α phase along the grain boundaries of prior β grains are observed (Fig. 5a and b). Micrographs recorded at higher magnification confirmed the formation of secondary α phases (α_s) in the β matrix (Fig. 5c and d).

Microstructural state of the Ti-10V-2Fe-3Al alloy after β recrystallisation treatment has revealed the formation of equiaxed prior β grains with intragranular lamellar α (Fig. 6). Formation of continuous α phase along most of the β grain boundaries are observed (labelled as 1 and 2 and shown as high magnification insets in Fig. 6a. The average grain size was calculated based on ASTM standard using individual optical micrographs. A histogram of the grain size distribution evaluated from optical micrographs revealed an average β grain size of ~ 450 µm (Fig. 6b). The high magnification micrographs display the formation of α layer at β grain boundaries. The β recrystallisation treatment resulted in nucleation of intergranular α colonies (α_{GB}) and growth of α phase within prior β grains (Fig. 7). SEM micrographs revealing basket weave grain structure and intragranular α phase nucleated and grown inside β2 and β3 grains, which can be related to post-heat treatment slow cooling rate.

3.2 High temperature flow behaviour of the Ti-10V-2Fe-3Al

The true stress-strain data obtained from the isothermal hot compression tests conducted at 720°C, 750°C and 780°C and under strain rates of $0.025s^{-1}$ and $0.2s^{-1}$ were analysed after correction for the machine compliance effect (Fig. 8). The graphs revealed an initial work hardening behaviour followed by flow softening upon further straining beyond the strain corresponding to the peak stress (ε_p) (Fig. 8a and b). The sharp peak in stress (σ_p) and the significant flow softening beyond the σ_p is a typical behaviour of titanium alloys with Widmannstatten/martensitic microstructure. An increase in σ_p with an increase in strain rate and a decrease in deformation temperature was observed (Fig. 8c). The magnitude of flow softening (S_{mag}) between ε_p and 0.8 strain (i.e., considered as the end of flow softening) was calculated based on an approach described by Semiatin et al., [16] as $S_{mag} = \Delta\sigma/\sigma_p$, where $\Delta\sigma = \sigma_p - \sigma_{(0.8)}$. A significant decrease in S_{mag} was observed (Fig. 8d) with increasing deformation temperature compared to the strain rate effect.

3.3 Microstructural evolution of the Ti-10V-2Fe-3Al alloy

The optical micrographs of the prior β grains following deformation to different reductions (i.e., 30%, 45% and 60%) at 750 °C and under 0.075 s^{-1} strain rate were analysed (Fig. 9). No significant changes to the grain morphology were observed for the sample deformed to 30% reduction (Fig. 9a). A gradual transformation of equiaxed prior β grains to an elongated morphology in the effective deformation zone was evident with increasing the percentage of reduction to 45% (Fig. 9b). Further increase in the deformation level to 60% reduction appeared to result in an increased homogeneity in grain morphology relative to the samples with less reduction (Fig. 9c). The negligible barrelling effect observed for all samples is an evidence of achieving uniform deformation up to 60% in reduction.

The orientation image maps of samples deformed to different levels of deformation were analysed using inverse pole figure (IPF) colouring with respect to the compression direction superimposed on their image quality maps (Fig. 10). The analyses revealed fragmentation of lamellar α with higher levels of deformation (i.e., 45% and 60%) (Fig. 10b and c) which is likely to be due to strain localisation followed by the formation of transverse boundaries as a result of dynamic recovery within the α lamellae. The presence of β subgrains with varying orientation are the evidence for dynamic recrystallisation (DRX) occurring in the prior β matrix with increased level of deformation (Fig. 10f). Diffusion assisted

globularisation of the fragmented and sheared α lamellae was also noticed in the microstructure of the samples deformed to 45% (Fig. 10c) and 60% (Fig. 10e). SEM analysis from the off-cut taken to forging temperature followed by water quenching confimed that the fraction of lamellar α present in the β matrix was around 17%.

The flow softening is a commonly observed phenomenon in titanium alloys during deformation at elevated temperatures. The flow softening phenomena exhibited by titanium alloys during uni-axial hot compression tests can be related to the microstructural changes as well as the temperature rise due to adiabatic heating during deformation. This can be due to the changes in the fraction and morphology of hard α phase caused by the combined effects of strain and temperature during deformation. Fragmentation of α lamellae leads to the globularisation of α, which is one of the key microstructural changes ocuring under the test conditions apart form the kinking and fragmentation. Two possible mechanisms for globularisation of α are reported by Zhao et al., [17]. The first mechanism is through diffussion assisted penetration of β phase into the deformed α lamellae leading to form cusps along the high angle α/α grain boundaries formed in deforming lamellar α phases. The formation of α/α grain boundaries within deformed α lamellae, are as a result of re-arrangement of dislocations generated within the α during deformation through dynamic recovery. The transverse boundaries formed within the deforming α lamellae acts as initiation sites for the fragmentation process by cusp formation process. The second mechanism of lamellar α fragmentation is by the migration of β phase along the shear bands generated within the favourably oriented α lamellae in the matrix. The formation of shear bands within lamellar α is due to localised shear deformation with its magnitude depending on the initial thickness of lamellar α [17]. Evidence of the early stages of lamellar α fragmention can be seen after 45% reduction (Fig. 10c). This is in comparison with the sample deformed to 30%, where most of the α lamellae appeared to be intact (Fig. 10b). Interestingly, the lamellar α has been fragmented into fine globular grains with less than 1 μm average diameter after 60% reduction (Fig. 10e).

The extent of deformation experienced by the β matrix depends on the aspect ratio of the constituent primary α phase. Globular α phase has been seen to have negligible influence on the deformation behaviour of β matrix compared to lamellar α phase. Further, the aspect ratio of lamellar α phase significantly impacts deformation behaviour of β matrix by hindering dislocation movements during deformation [17]. The observed flow softening at all deformation temperatures can be attributed to the microstructural refinement of α phase.

Further, steep flow softening beyond the peak stress can also be related to the fragmentation of lamellar primary α followed by morphological changes of globular α particles [18]. In this study, the effect of adiabatic temperature was considered as negligible due to the low strain rates (i.e., 0.025 - 0.2 s^{-1}). Therefore, the observed flow softening can predominantly be due to the microstructural changes occurring during hot deformation.

The extent of dynamic recrystallisation occurring in the lamellar α and in the β matrix as a function of percentage of reduction during hot compression tests are analysed (Fig. 11). The increase in the strain level has led to an increase in the fraction of deformed grains in α phase (Fig. 11a, c and e), where the majority of lamellar α underwent fragmentation beyond 45% reduction. Dynamic recovery appears to occur in the β matrix during deformation for all samples. The recrystallisation fraction maps suggest that the level of dynamic recovery increases with higher deformation level (Fig. 11b, d and f). It was noticed that the size and morphology of α phase and the separation distance between α grains have direct influence on the deformation characteristics of the β matrix. The fraction of β undergoing dynamic recovery increases with an increase in strain, and the increase in fraction of globular α phase beyond 30% reduction as a function of deformation level leads to a switch in the recovery mechanism in β matrix from dynamic recovery to dynamic recrystallisation. An increase in the recrystallised β fraction from ~12% to ~55% is observed with an increase in the percentage of deformation from 30 to 60 % (Fig. 11b, d and f). On the other hand, the decrease in the fraction of grains with sub-structure from ~80% to ~38% suggests the transformation of the deformed grains to recrystallised grains in β matrix with an increase in the percentage of reduction. The extent of metadynamic and static recrystallisation were assumed to be suppressed largely by water quenching of the samples following the compression tests. Thus, the increase in the fraction of sub-grains in the β matrix is due to dynamic recrystallisation and can be related to the flow softening behaviour exhibited by the true stress - true strain curves (Fig. 8).

4.0 Discussion

4.1 Analysis of the activation energy for deformation

The plots of true stress versus true strain obtained from the hot compression tests were used to calculate the activation energy for deformation in each case (Fig. 8a and b). The temperature and strain rate are the key parameters controlling the flow behaviour during hot compression tests. For these analyses, an Arrhenius based constitutive equation was used to

describe the relationship between flow stress (σ), strain rate ($\dot{\varepsilon}$) and temperature (T) (Equation 1) [19].

$$Z = \dot{\varepsilon} \exp\left(\frac{Q}{RT}\right) \quad (1)$$

$$\dot{\varepsilon} = AF(\sigma) \exp\left(-\frac{Q}{RT}\right) \quad (2)$$

where,

$$F(\sigma) = \begin{cases} \sigma^{n_1} & \alpha\sigma < 0.8 \text{ (for low stress level)} \\ \exp(\beta\sigma) & \alpha\sigma > 1.2 \text{ (for high stress level)} \\ [\sinh(\alpha\sigma)]^{n_2} & for\, all\ \sigma \text{ (for } all\ stress\ levels) \end{cases}$$

In Equation 1, Q is the activation energy for deformation (J mol^{-1}), R is the universal gas constant (8.3145 J mol^{-1} K^{-1}), n is the strain hardening coefficient, α is the stress magnitude parameter ($\alpha = \beta/n$), and A is a material constant. The equations presented in (1) and (2) can change shape depending on strain, which is a function of the stress magnitude. For instance, $F(\sigma)$ value varies depending on the stress magnitude (i.e., low or high) which results in Equation (2) taking alternative forms as Equations (3) and (4),

$$\dot{\varepsilon} = B\sigma^{n_1} \quad (3)$$

$$\dot{\varepsilon} = C \exp(\beta\sigma) \quad (4)$$

where, B and C are material constants. Equations (3) and (4) have then been reshaped into logarithmic coordinate as Equations (5) and (6) to present the stress-strain relationship as linear curves.

$$\ln(\sigma) = \frac{1}{n_1}\ln(\dot{\varepsilon}) - \frac{1}{n_1}\ln(B) \quad (5)$$

$$\sigma = \frac{1}{\beta}\ln(\dot{\varepsilon}) - \frac{1}{\beta}\ln(C) \quad (6)$$

Thus, the material constants n_1 and β can be obtained from averaging the inverse slopes of the $\ln(\sigma)$ versus $\ln(\dot{\varepsilon})$ curve (Fig. 12a) and σ versus $\ln(\dot{\varepsilon})$ curve for different temperatures (Fig. 12b), respectively. The value of $\alpha = \frac{\beta}{n_1} = \frac{0.031}{5.2}$ is 0.0059 MPa^{-1}.

Substituting the value of $F(\sigma)$ for all the stress levels into Equation (2) yields,

$$\dot{\varepsilon} = A\,[\sinh(\alpha\sigma)]^{n_2} \exp\left(-\frac{Q}{RT}\right) \quad (7)$$

Similarly, Equation (7) can be reshaped into logarithmic scale as,

$$\ln[\sinh(\alpha\sigma)] = \frac{\ln(\dot{\varepsilon})}{n_2} + \frac{Q}{n_2 RT} - \frac{\ln A}{n_2} \quad (8)$$

Thus, for a constant deformation temperature and strain rate, differentiating Equation (8) leads to Equation (9):

$$\frac{1}{n_2} = \frac{d\{\ln[\sinh(\alpha\sigma)]\}}{d\{\ln(\dot{\varepsilon})\}} \quad (9)$$

and,

$$Q = n_2 R \, \frac{d\{\ln[\sinh(\alpha\sigma)]\}}{d(1/T)} \quad (10)$$

The values of n_2 and A were obtained from the average inverse slope and the intercept of $\ln[\sinh(\alpha\sigma)]$ versus $\ln(\dot{\varepsilon})$ curve for different temperatures (Fig. 12c). Consequently, the average activation energy for deformation was calculated as 487 kJmol^{-1} at ε_p for varying strain rates and temperatures (Fig. 12d). The increase in volume fraction of β phase with the working temperature approaching β-transus has resulted in dynamic recovery. This is due to the accommodation of deformation mainly by β phase, where α phase acts as hard particles dispersed in a soft β matrix [2]. The activation energy for dynamic recovery is mainly at lower ranges close to the activation energy for β working. However, a relatively high activation energy at ε_p calculated for the present study suggests a high potential for dynamic recrystallisation. In previous studies on the same material, activation energy reported by Robertson et.al. [2], was 297 kJmol^{-1}, and Balasubrahmanyam et. al. [14] was 225 kJmol^{-1} and 320 kJmol^{-1} for tests carried out under strain rates below and above 0.1 s^{-1}, respectively. Both authors reported the activation energy for a steady state stress leading to a potentially dynamic recovery at the forging temperature.

4.2 Model descriptions for predicting flow behaviour

The active mechanisms during hot working of a material can typically be divided into work hardening, dynamic recovery and dynamic recrystallisation. The increase in dislocation density and dislocation motion as a result of the applied strain results in plastic deformation which can constitutes work hardening, steady state plastic deformation and flow softening, depending on material properties [20]. The flow softening beyond the ε_p can occur due to dynamic recovery and the annihilation of the geometrically necessary dislocations generated at the earlier stages of the deformation [21].

Kocks and Mecking [22] have developed a relationship to link the dislocation density (ρ) and the deformation stress (σ) to the strain rate ($\dot{\varepsilon}$) and deformation temperature (T). The quantitative determination of work hardening of the alloy has been calculated at a constant strain rate and temperature from the slope of true stress-true strain curves according to Equation 11 and Fig. 13. No significant difference was observed between the work hardening

rates for varying strain rates and deformation temperatures. The work hardening rate is described as,

$$\theta = \frac{\partial \sigma}{\partial \varepsilon}\Big|_{\dot{\varepsilon}T} \tag{11}$$

where θ is the work hardening rate. Further, Kocks and Mecking [22] have developed a linear relationship between the work hardening rate and flow stress as Equation 12.

$$\theta = \theta_0 \left(1 - \frac{\sigma}{\sigma_s}\right) \tag{12}$$

where $\theta_0 = \alpha G b k_1/2$ and saturation stress, $\sigma_s = \alpha G b (k_1/k_2)$. The saturation stress can also be experimentally measured as the point at which a tangent to the plot of work hardening rate curve versus true stress becomes minimum (i.e., θ = 0). Line drawn to calculate saturation stress for the sample tested at 720˚C at 0.2 s^{-1} is shown in Fig. 13b. In which the tangent to the slope of the curves, in which α is a material constant, G is the shear modulus, b is the magnitude of burger's vector, k_1 is a constant associated with thermal storage of moving dislocations, and k_2 is a constant associated with the annihilation of dislocations. Estrin and Mecking [23] (EM) further modified the Kocks-Mecking model and established the relationship as,

$$\theta\sigma = A - B\sigma^2 \tag{13}$$

Integrating Equation 13, over a deformation range, assuming a constant strain rate, yields Equation 14.

$$\sigma^{EM} = \left[\sigma_s^2 + (\sigma_0^2 - \sigma_s^2)\exp(-2B\varepsilon)\right]^{1/2} \tag{14}$$

where σ_0 is the initial stress, and A and B are the constants associated with the Zener-Hollomon parameter.

Converting Equation 14 into a logarithmic scale takes the form of Equation 15.

$$\ln(\sigma_s^2 - \sigma^2) = \ln(\sigma_s^2 - \sigma_0^2) - 2B\varepsilon \tag{15}$$

The optimum σ_0 and B were obtained from the best fit to $\ln(\sigma_s^2 - \sigma^2)$ versus ε curve presented in Fig. 14a.

The dislocation density augumentation based EM model can predict the work hardening behaviour up to ε_p. To predict the flow softening beyond ε_p, Kong et al., [24] combined the Avrami equation with Equation 14 and defined as Equation 16 taking into consideration the dynamic recrystallisation, which is refered to as the EM+Avrami model hereafter.

$$\sigma = \sigma^{EM} - X\,(\sigma_s - \sigma_{ss}),\ for\ \varepsilon > \varepsilon_p \quad (16)$$

where σ^{EM} is the true stress predicted by the EM model (Equation 14), X is the fraction of dynamic recrystallisation at a specific strain ($0 < X \leq 1$), and σ_{ss} is the steady state stress (i.e., at 0.8 strain) (highlighed in Fig. 8a). The fraction of recrystallisation at every strain is then expressed as:

$$X = \frac{\sigma^{EM} - \sigma}{\sigma_s - \sigma_{ss}} = 1 - \exp(-a(\varepsilon - \varepsilon_p)^b) \quad (17)$$

and

$$\ln(-\ln(1 - X)) = \ln a + b \ln(\varepsilon - \varepsilon_p) \quad (18)$$

The constants a and b were respectively determined from the intercept and slope of the $\ln(-\ln(1 - X))$ versus $\ln(\varepsilon - \varepsilon_p)$ curve for $\varepsilon > \varepsilon_p$, presented in (Fig. 14b). Minor variations in the material constants were observed for different temperatures and strain rates (Fig. 12b). However, in order to reduce the complexity of the model, the material constants were considered to be the same for all strain rates and temperatures (Table 2). Moreover, the model independency has been increased by calculating the σ_s, σ_{ss} and ε_p constants as functions of Zener-Hollomon parameter (Z) presented in Equation 1. A power law function was considered as a best fit for the constants with Z and therefore used to calculate σ_s, σ_{ss} and ε_p as a function of log (Z) (Fig. 15).

4.3 Validation of the material model

The generalised EM+Avrami model developed in this study (Equation 14 and 16) was used to predict the flow behaviour in the Ti-10V-2Fe-3Al alloy at different temperatures and a range of strain rates. This includes the work hardening and flow softening over the investigated temperatures and strain rates (Fig. 16). An uncertainty was associated with the results of the model prediction for flow softening at low temperatures and under the slowest strain rate, and also at high temperatures and under high strain rate conditions (Fig 16). These uncertainties at extreme conditions are related to the large errors associated with the materials constants (i.e., σ_s, σ_{ss} and ε_p) evaluated via curve fitting (Fig. 15) and averaging the constants B, a and b (Fig. 14). These uncertainties can be corrected by calculating the material's constants independently as a function of test parameters (i.e., strain rate and temperature). However, the model has revealed high degree of accuracy under intermediate strain rates for all deformation temperatures (Fig. 16b and c). Therefore, the developed

EM+Avrami model was considered as a suitable mean of predicting hot deformation behaviours in the Ti-10V-2Fe-3Al alloy with uniform material constants for all processing conditions.

The accuracy of prediction was analysed by comparing the predicted and measured flow stress values and by calculating the correlation coefficient (R^2) for all process conditions. The R^2 value was found to be 96.54%, confirming a good correlation between the results of experiments and those of the proposed model (Fig. 15d).

4.4 Simulation of the open-die forging process

The forging industries are keen on developing innovative manufacturing methods and improving their existing procedures to produce parts with better quality at reduced cost. Thus, eliminating the experimental procedures, which often involves multiple trials and errors with highly accurate process simulation models present challenges. A combination of material information and process simulation capabilities has proved to help the forging industry to manufacture products with tailored properties. FE simulation tools capable of using various empirical, semi empirical and physically based material models to predict hot deformation behavior of various alloys, have been developed and reported by various studies [7, 10]. Considering the necessity for an accurate material model for predicting the hot deformation in Ti-10V-2Fe-3Al alloy, an effort is made to incorporate the developed EM+Avrami model into the commercially available DEFORM® 3D software package. Accordingly, an in-house user subroutine was developed to integrate the EM+Avrami model into the DEFORM FE package for predicting the deformation behavior in Ti-10V-2Fe-3Al alloy during open-die forging process. The simulated results were then validated using the results of experimental forging trails.

A non-isothermal hot open die forging simulation on a cube with 105×105×105 mm, using material properties for Ti-10V-2Fe-3Al was set up in DEFORM (Fig. 17). To minimise the simulation time, a deformable work piece and rigid dies were considered. The workpiece was meshed with tetrahedral elements to a minimum mesh size of 2 mm at the edges and maximum mesh size of 5 mm at the core. The workpiece was soaked at the forging temperature of 750 ˚C, followed by 15 seconds transfer in air to replicate the cube transfer from a furnace to the forging press by applying heat transfer coefficient with air (Fig. 17 a). The friction between the dies and interacting surfaces of the cube was considered as a lubricated hot forging condition with a friction coefficient (μ) of 0.2. The heat transfer

coefficient (HTC) between the workpiece and dies was maintained constant as 1 N/sec/mm/°C. The temperature of the top and bottom dies were kept at ~ 400 ˚C. The top die movement was considered as a function of time to achieve the adopted experimental strain rate. The speed used for the experimental forging was adopted to maintain strain rate ~ 0.075 s^{-1}. The simulation was used to predict the strain distribution, temperature raise due to adiabatic heating, shape change and the load required to forge the cubic samples to three different levels of reduction. Finally, the simulated results were validated using the results of forging trials.

4.4.1 Validation of the results of FE simulation

The results of open die forging FE simulations were then compared with the results of forged cubes. The results for all levels of reduction (i.e., 30%, 45% and 60%) were compared with the measured shape and dimensions of the forged parts. The 3D geometry of the forged cubes was obtained using 3D optical scanning and the results were compared to those of the FE simulations for dimensional accuracy (Fig. 18). The simulated results show a good accuracy in the prediction of dimensions based on the implemented material's flow behaviours. The maximum bulge dimension was measured and compared with the simulated results. The FE simulations were able to predict the maximum bulging level for all three deformation levels with negligible uncertainties. These analyses show a maximum error of less than 1% for the cube geometry forged to various levels of reduction.

4.4.2. Analysis of friction contact region

To understand the effect of friction on the forged cubes further, a dimensional measurement indicating the extent of friction over the contact region between the workpiece and the dies, was carried out on the 3D models obtained by optical measurement (i.e., GOM ATOS) (Fig. 19a). The extent of experimentally measured dimensional changes for all levels of deformation in comparison with the original cube just before forging is summarised in Fig. 19b. To compare the data with the results of FE simulations, data were also collected from the FE models using point-tracking method. For this purpose, points have been marked at four corners of the models and their displacements were measured throughout the forging simulation with an increase in the reduction level (Fig. 19c). The point tracking results confirmed an expansion of the friction contact region with an increase in the level of deformation. An increase in the friction contact region from 105 mm to 125 mm for the cube forged to 60% reduction suggests that the delta glaze coating and synthetic graphite lubricant used during the experimental forging trials might have resulted in significant reduction in

friction and also the loss of temperature at die billet interface (Fig. 19b). The results of FE simulation has revealed fairly high accuracy in predicting the expansion of the friction contact regions with the $\mu = 0.2$ and heat transfer coefficient of 1 N/sec/mm/°C (Fig. 19c). A maximum error of ~ 4 % was observed for the cube forged to 60% reduction. The relatively high accuracy obtained in friction contact region analysis suggests that the FE simulation has been successful in adopting the actual forging conditions.

4.4.3 Analysis of the effective strain distribution and grain flow

Analyses of the predicted effective strain distributions in the forged cubes substantiate the existence of large dead zones near the bottom and top faces of the cubes. The maximum predicted magnitudes of effective strain developed during forging to 30%, 45% and 60% reduction were ~ 0.94, ~ 1.44 and ~ 1.93, respectively (Fig. 20). To understand the grain flow behaviour, 5mm thick slices were machined out of the forged cubes for analyses using OM (Fig. 20). The optical micrographs of all three forged cubes clearly show the effective strain zones (i.e., the core) and the dead zones (i.e., top and bottom) through noticeable differences in the microstructure evolution of prior β grains. The areas of strain localisation and the dead zones on top and bottom of the cubes predicted by the FE simulation (Fig. 20a, b and c) can be distinguished through the observed differences in grain flow after forging trials. Equiaxed prior β grains in the areas with high effective strain have become elongated and deformed perpendicular to the direction of loading (i.e., in compression) under the influence of the geometrically necessary tensile forces generated perpendicular to the loading direction during compressive deformation. A combination of tensile and compressive forces has led to the flow of prior β grains at 45° angle to the loading direction close to the dead zones. This is primarily due to the activation of shear stresses under the influence of tensile and compressive forces. Evidence for flow of β grains due to shear deformation is distinctly seen in optical micrographs after 45% and 60% reductions (highlighted in Fig. 20b and c).

4.4.4 Analysis of the predicted forging load

The suitability of the proposed material model for industrial applications was evaluated by comparing the predicted forging load with the load measured during the open die forging trials. These are plotted against the top die displacement throughout the forging durations and shown in Fig. 21. The model shows a high level of accuracy in predicting the load required for forging of the cubes up to 60% reduction. A maximum error of ~ 9% higher predicted

load was observed at 60% reduction. This can be related to the error accumulated due to the generalisation of materials constants used in Equation 14 and 17.

The developed EM + Avrami based constitutive material model was suitable for sub-transus working temperatures (i.e., from 720 °C to 780 °C) of the Ti-10V-2Fe-3Al alloy. The open die forging simulations carried out at 750 °C revealed an increase in temperature due to adiabatic heating for all the three levels of deformation (Fig. 21). The temperature due to adiabatic heating increased to ~ 793 °C) close to β-transus (i.e. ~795 °C) for the forging trial with deformation level reaching 60% reduction. The maximum temperature rise was limited to a small area in the middle of the FE model. This suggests that the temperature range might have exceeded the predicting capacity of the material model developed in this study which potentially change the microstructure evolution mechanism from dynamic recrystallisation to dynamic recovery near or above the β-transus [14]. However, the model continues to predict the deformation behaviour based on the constitutive equations developed for sub-transus temperatures. This can be corrected by extending the working range of EM+Avrami model to higher temperatures.

An analysis has been carried out to understand the difference between the developed EM+Avrami material model and the existing DEFORM material database. The results of comparison show that the FE prediction by using EM+Avrami material model is closer to the experimentally measured data (Fig. 21). Thus, the developed EM+Avrami model is a good tool to be incorporated in FE packages such as DEFORM®3D for sub-transus forging simulation of Ti-10V-2Fe-3Al alloy. The developed material model can effectively be used for the prediction of 3D flow behaviours during industrial forging operations such as upsetting and cogging.

5.0 Conclusion

In this study, deformation behaviour of Ti-10V-2Fe-3Al alloy, during iso-thermal compressions under different strain rates at various sub-transus temperatures, and the associated microstructural evolutions were investigated. A constitutive material model was developed by extending previous models, namely Estrin-Mecking and Avrami (EM+Avrami), based on the results of compression tests. The developed EM+Avrami based constitutive model was successfully incorporated into DEFORM®3D FE package as a material subroutine. The material's constitutive descriptions were seen to enhance the

accuracy of the results of FE simulations of open die forging process. The main outcomes of this study are summarised in the following:

- High temperature working below β-transus of Ti-10V-2Fe-3Al alloy with an initial lamellar microstructure exhibited significant work hardening at early stages of deformation, followed by flow softening beyond a peak stress which tends towards a steady state stress after ~ 60% reduction.
- Microstructural findings suggest that the flow softening can be due to the globularisation of fragmented primary α lamellae within the β matrix. Also, the steady state flow can be related to the dynamic recrystallisation of β grains, and stress induced morphological changes in lamellar α phase. Evidence of microstructural evolution were gained from compression tests after different levels of deformations (i.e., 30% and 45% reduction).
- A new constitutive material model (EM+Avrami) with reduced constants was developed with over 95% accuracy in predicting sub-transus flow behavior of Ti-10V-2Fe-3Al alloy.
- The results of FE simulations, taking into consideration the developed EM+Avrami constitutive material model as a user subroutine, showed enhanced accuracy in predicting the dimensions, bulging, strain distribution and forging load during open die forging.

Author Statement

Name	Definition
Paul M Souza	Constitutive analysis and FE simulation, Manuscript preparation.
Giribaskar Sivaswamy	Conceptualization of the project, Experimental planning, Experimental analysis, Results Analysis, Manuscript preparation.
Liza Hall	Experimental analysis, Results Analysis.
Salaheddin Rahimi	Results Analysis, Manuscript writing and reviewing.

Declaration of interests

The authors declare that they have no known competing financial interests or personal relationships that could have appeared to influence the work reported in this paper.

Acknowledgements

The authors would like to acknowledge the support provided by TIMET, Aubert & Duval and Bifrangi for this project. The authors sincerely thank Mr. Yvon Millet, TIMET Savoie, France for the technical discussions throughout the project and Dr. Kayla Calvert, TIMET USA for reviewing the manuscript. The experimental works were carried out at the Advanced Forming Research Centre (AFRC), University of Strathclyde, which receives partial financial support from the UK's High Value Manufacturing CATAPULT.

References

[1] M. Jackson, R. Dashwood, L. Christodoulou, H. Flower, The Microstructural Evolution of Near Beta Alloy Ti-10V-2Fe-3Al during Subtransus Forging, Metal. Mater. Trans. A, 36A, (2005), 1317.

[2] D.G. Robertson, H.B. McShane, Analysis of high temperature flow stress of titanium alloys IMI 550 and Ti-10V-2Fe-3AI during isothermal forging, Mater. Sci. Tech., 14(4), (1998), 339-345.

[3] G.T. Terlinde, T.W. Duerig, J.C. Williams, Microstructure, tensile deformation, and fracture in aged ti 10V-2Fe-3Al, Metal. Trans. A, 14(10), (1983), 2101-2115.

[4] Y.C. Lin, X.-M. Chen, A critical review of experimental results and constitutive descriptions for metals and alloys in hot working, Mater. Des. 32(4) (2011) 1733-1759.

[5] L.X. Kong, P.D. Hodgson, D.C. Collinson, Extrapolative prediction of the hot strength of austenitic steels with a combined constitutive and ANN model, J Mater. Proces. Tech., 102(1–3), (2000), 84-89.

[6] B. Babu, L.-E. Lindgren, Dislocation density based model for plastic deformation and globularization of Ti-6Al-4V, Int. J Plas., 50, (2013), 94-108.

[7] P.M. Souza, J. Mendiguren, Q. Chao, H. Beladi, P.D. Hodgson, B. Rolfe, A microstructural based constitutive approach for simulating hot deformation of Ti6Al4V alloy in the $\alpha + \beta$ phase region, Mater. Sci. Engg. A, 748, (2019), 30-37.

[8] R. Julien, V. Velay, V. Vidal, Y. Dahan, R. Forestier, F. Rézaï-Aria, Characterization and modeling of forged Ti-6Al-4V Titanium alloy with microstructural considerations during quenching process, Int. J Mech. Sci., 142-143, (2018), 456-467.

[9] V. Velay, H. Matsumoto, V. Vidal, A. Chiba, Behavior modeling and microstructural evolutions of Ti–6Al–4V alloy under hot forming conditions, Int. J Mech. Sci., 108-109, (2016), 1-13.

[10] R. Bobbili, B. Venkata Ramudu, V. Madhu, A physically-based constitutive model for hot deformation of Ti-10-2-3 alloy, J Alloy. Compd., 696, (2017), 295-303.

[11] E. Buzaud, L. Li, X. Zhang, Z. Li, Z. Wang, W. Ma, A. Cosculluela, H. Couque, E. Cadoni, The mechanical behaviours of the Ti-10V-2Fe-3Al alloy under the high-temperature and dynamic loading conditions, EPJ Web of Conferences, 183, (2018).

[12] H. Zhan, G. Wang, D. Kent, M. Dargusch, Constitutive modelling of the flow behaviour of a β titanium alloy at high strain rates and elevated temperatures using the Johnson–Cook and modified Zerilli–Armstrong models, Mater. Sci. Engg. A, 612, (2014), 71-79.

[13] P.M. Souza, H. Beladi, R.P. Singh, P.D. Hodgson, B. Rolfe, An Analysis on the Constitutive Models for Forging of Ti6Al4V Alloy Considering the Softening Behavior, Int. J Mater. Engg. Perform., 27(7), (2018), 3545-3558.

[14] V.V. Balasubrahmanyam, Y.V.R.K. Prasad, Hot deformation mechanisms in metastable beta titanium alloy Ti–10V–2Fe–3Al, Mater. Sci. Tech., 17(10), (2001), 1222-1228.

[15] D. Palousek, M. Omasta, D. Koutny, J. Bednar, T. Koutecky, F. Dokoupil, Effect of matte coating on 3D optical measurement accuracy, Optic, Mater., 40, (2015), 1-9.

[16] S.L. Semiatin, V. Seetharaman, I. Weiss, Flow behavior and globularization kinetics during hot working of Ti–6Al–4V with a colony alpha microstructure, Mater. Sci. Engg. A, 263(2), (1999), 257-271.

[17] J. Zhao, J. Zhong, M. Zhou, F. Chai, F. Yan, The effect of alpha phase on flow softening and deformation of Ti–10V–2Fe–3Al, Mater. Sci. Tech., 33(16), (2017), 1993-2003.

[18] M. Jackson, N.G. Jones, D. Dye, R.J. Dashwood, Effect of initial microstructure on plastic flow behaviour during isothermal forging of Ti–10V–2Fe–3Al, Mater. Sci. Engg. A, 501(1-2), (2009), 248-254.

[19] C. Zener, J. Hollomon, Effect of strain rate upon plastic flow of steel, J App. Phy., 15(1), (1944), 22-32.

[20] P. Castany, F. Pettinari-Sturmel, J. Crestou, J. Douin, A. Coujou, Experimental study of dislocation mobility in a Ti–6Al–4V alloy, Acta. Mater., 55(18), (2007), 6284-6291.

[21] S.H. Zahiri, C.H.J. Davies, P.D. Hodgson, A mechanical approach to quantify dynamic recrystallization in polycrystalline metals, Scri. Mater., 52(4), (2005), 299-304.

[22] H. Mecking, U.F. Kocks, Kinetics of flow and strain-hardening, Acta. Metal., 29(11), (1981), 1865-1875.

[23] Y. Estrin, H. Mecking, A unified phenomenological description of work hardening and creep based on one-parameter models, Acta. Metal., 32(1), (1984), 57-70.

[24] L.X. Kong, P.D. Hodgson, B. Wang, Development of constitutive models for metal forming with cyclic strain softening, J Mater. Proces. Tech., 89–90(0), (1999), 44-50.

(a)

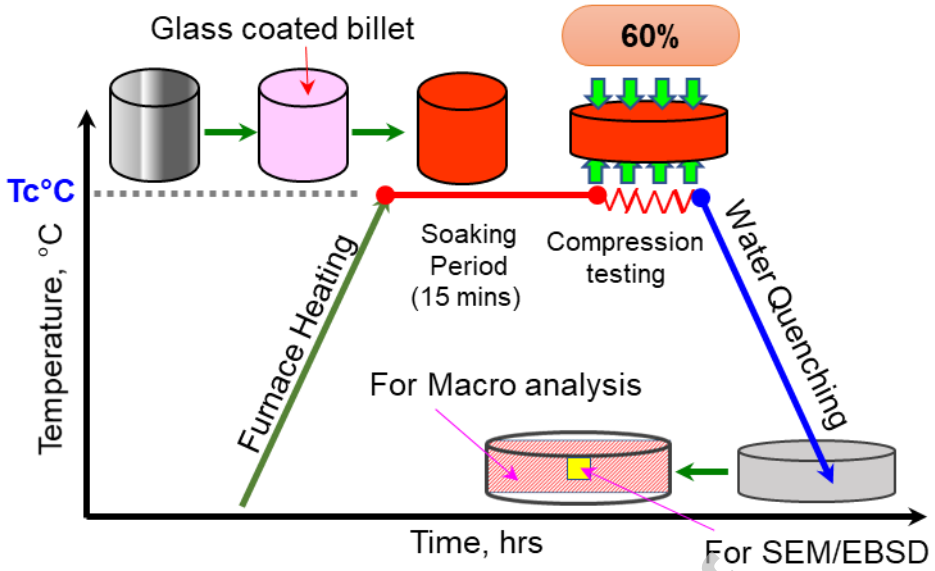

(b)

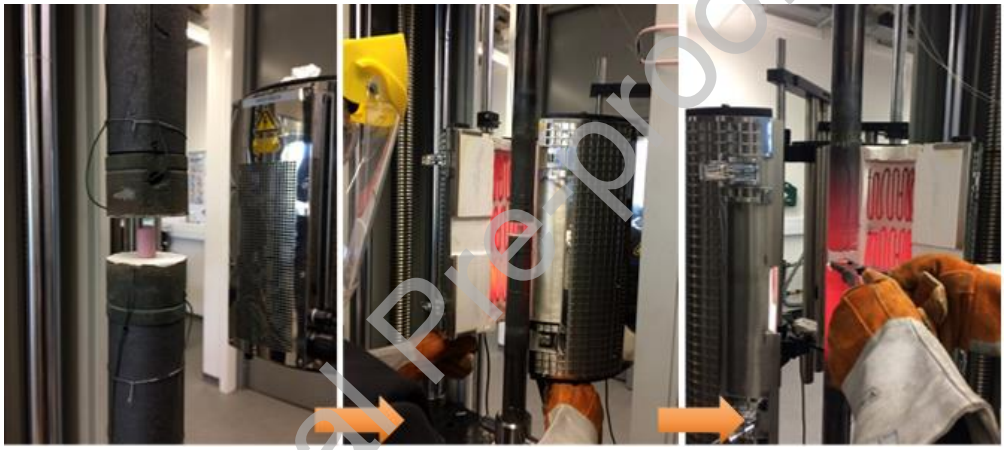

Figure 1: (a) Schematic representation of the hot compressions test and (b) Photographs showing different stages of a test. Tc is the compression test temperature.

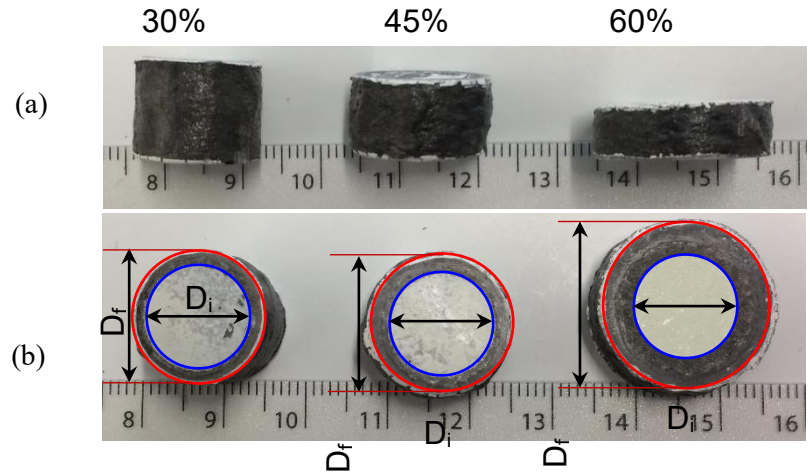

Figure 2: (a) Photographs showing front views of the samples after 30%, 45% and 60% reductions at 750°C, under the strain rate of 0.075 s^{-1} followed by water quenching, and (b) Photographs showing the top views of the same samples with superimposed circles showing the initial (Blue) and the final (Red) peripheries (D_i and D_f are initial and final diameter of samples).

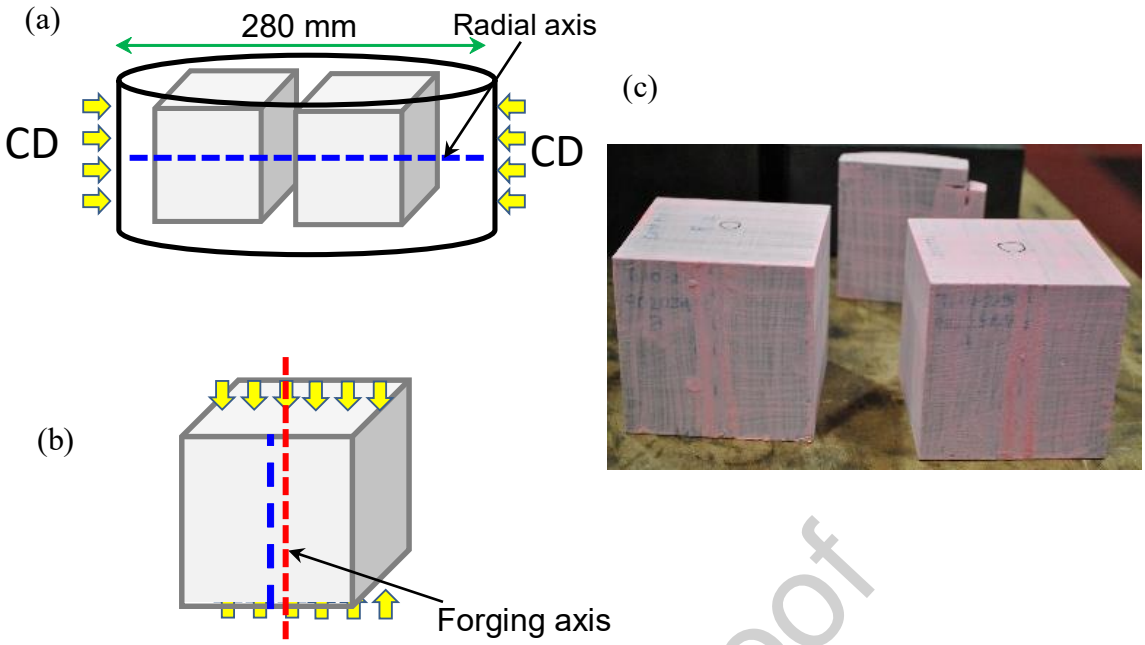

Figure 3: (a) Schematic showing the locations of the cubes machined from the as-received cogged billets of Ti-10V-2Fe-3Al alloy, (b) Schematic showing the forging direction with respect to the CD of the as-received billet (i.e., highlighted in dotted blue line), and (c) A photograph showing the machined and delta-glaze coated cubic samples.

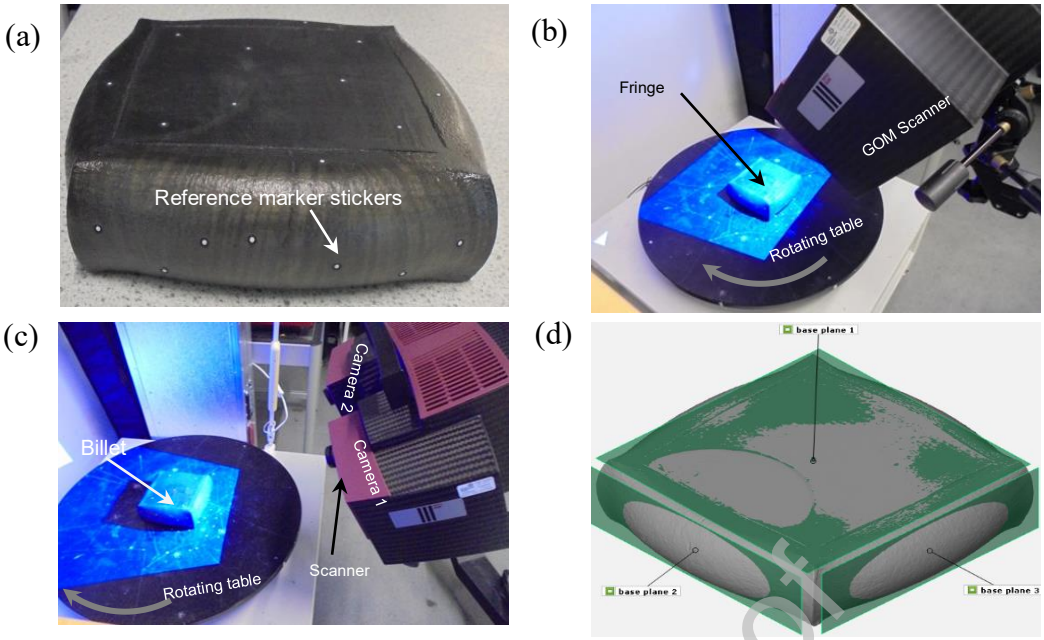

Figure 4: Photographs illustrating the steps involved in 3D scanning of the forged samples using GOM -ATOS, (a) sticking reference markers to the surfaces of a forged cube, (b, c) scanning and acquisition of images from the cubes placed on a rotating table, and (d) a reconstructed 3D model of a forged part.

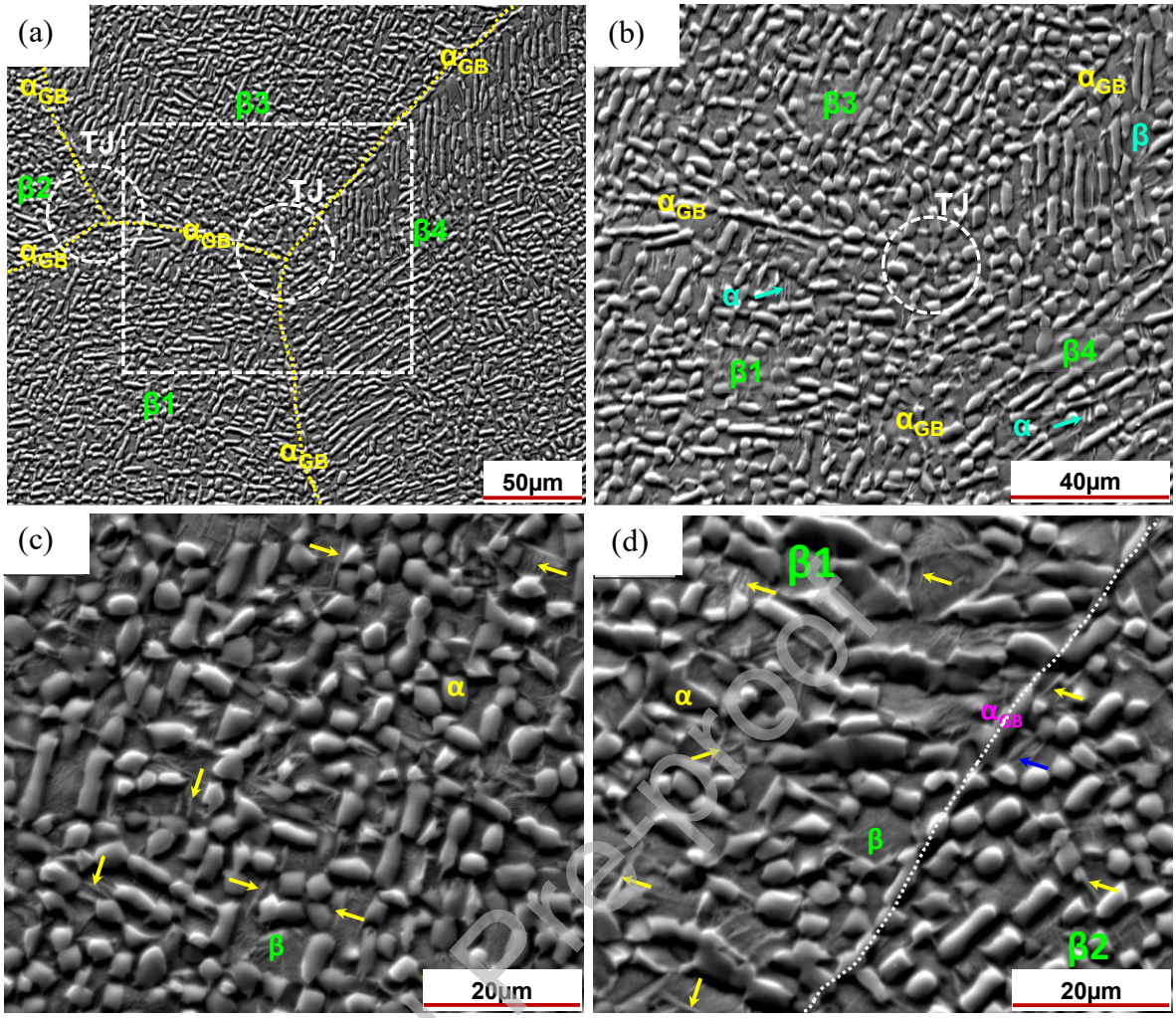

Figure 5: (a) and (b) SEM micrographs of the as-received billet, taken at different magnification, showing lamellar and globular α phase within primary β grains (α_{GI}) with continuous and discontinuous primary α phase along the grain boundaries (α_{GB}). (c) and (d) Evidence of the formation of secondary α phase (α_s) in the β matrix (yellow arrows) and along the prior β grain boundary (highlighted as a white dotted line).

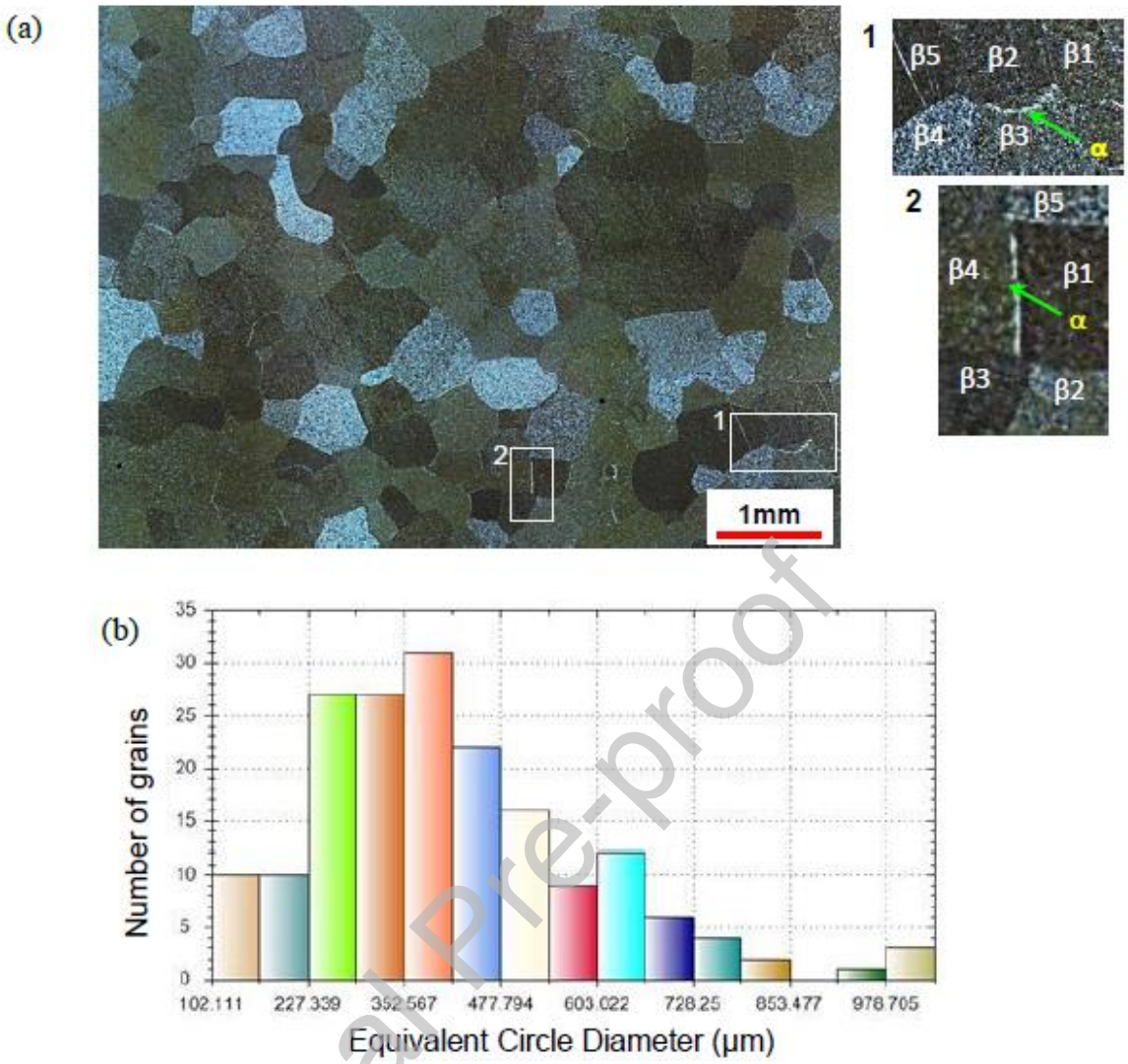

Figure 6: (a) An optical micrograph of the billet after the β recrystallisation treatment. Location 1 and 2 are highlighting continuous α along β grain boundaries in the high magnification insets. (b) Histogram showing the β grain size distribution evaluated from optical micrographs.

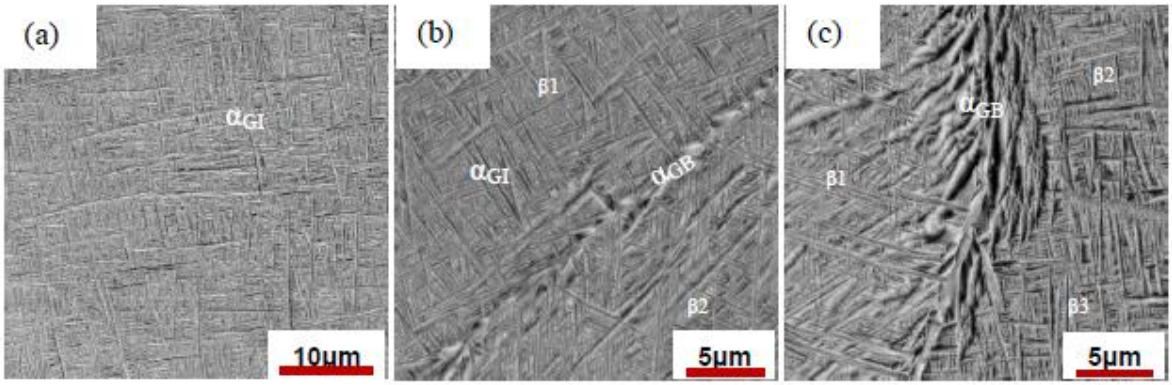

Figure 7 :(a) to (c) SEM micrographs showing microstructural characteristics of the Ti-10V-2Fe-3Al alloy after β recrystallisation treatment.

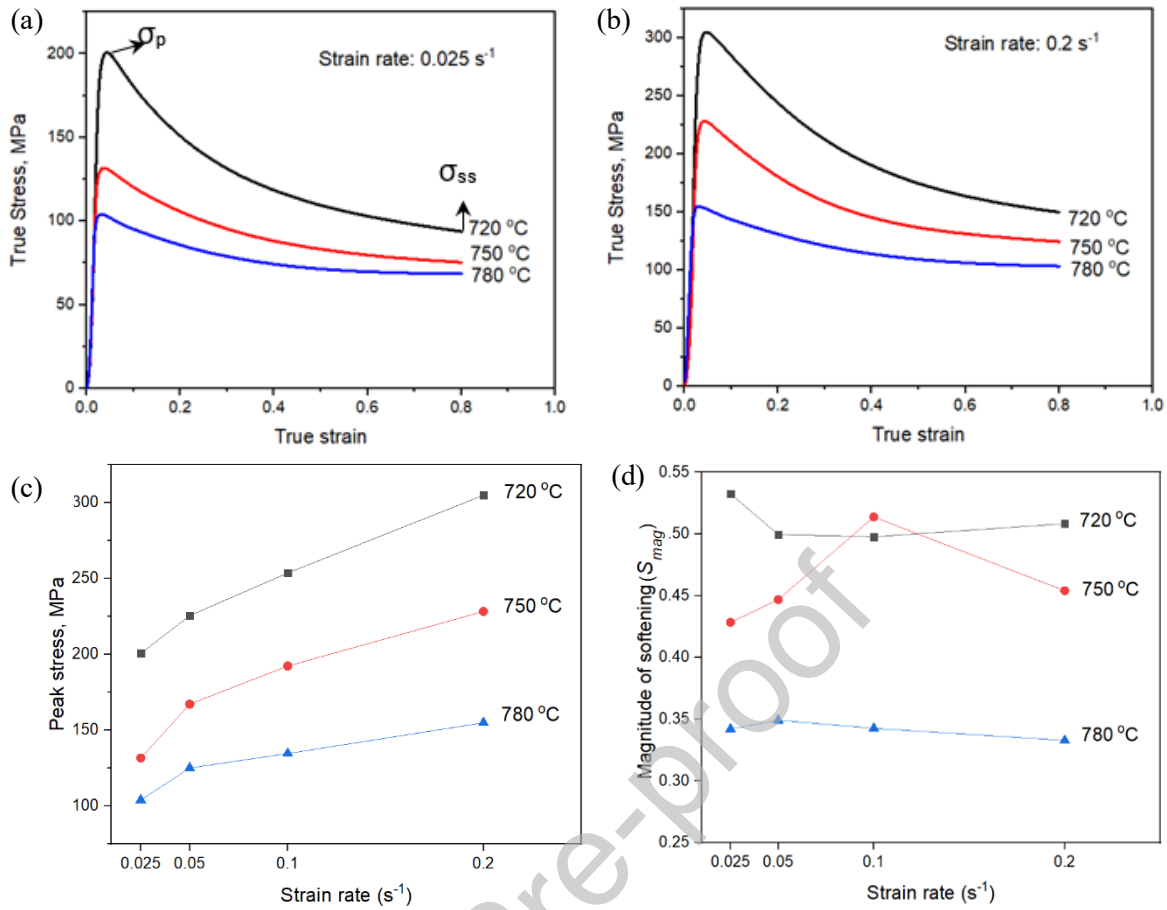

Figure 8: True stress vs. true strain curves measured for the Ti-10V-2Fe-3Al alloy at three test temperatures under strain rate of (a) 0.025 s^{-1}, and (b) 0.2 s^{-1}, (c) variation in peak stress with varying temperature and strain rate, and (d) variation in magnitude of softening with varying temperature and strain rate. σ_p and σ_{ss}, highlighted on the curves in (a), are the peak stress and steady state stress, respectively.

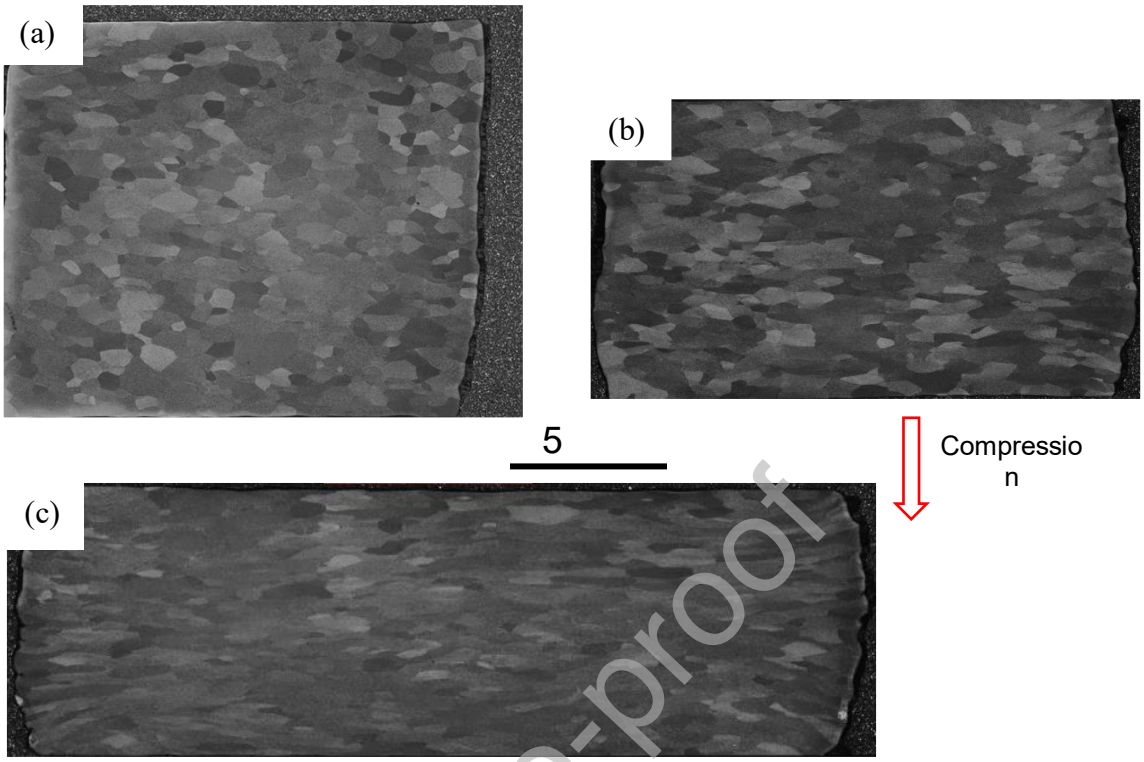

Figure 9: Optical micrographs of the cylindrical samples tested in compression at 750 °C under 0.075 s^{-1} strain rate to different levels of deformation (a) 30%, (b) 45% and (c) 60%.

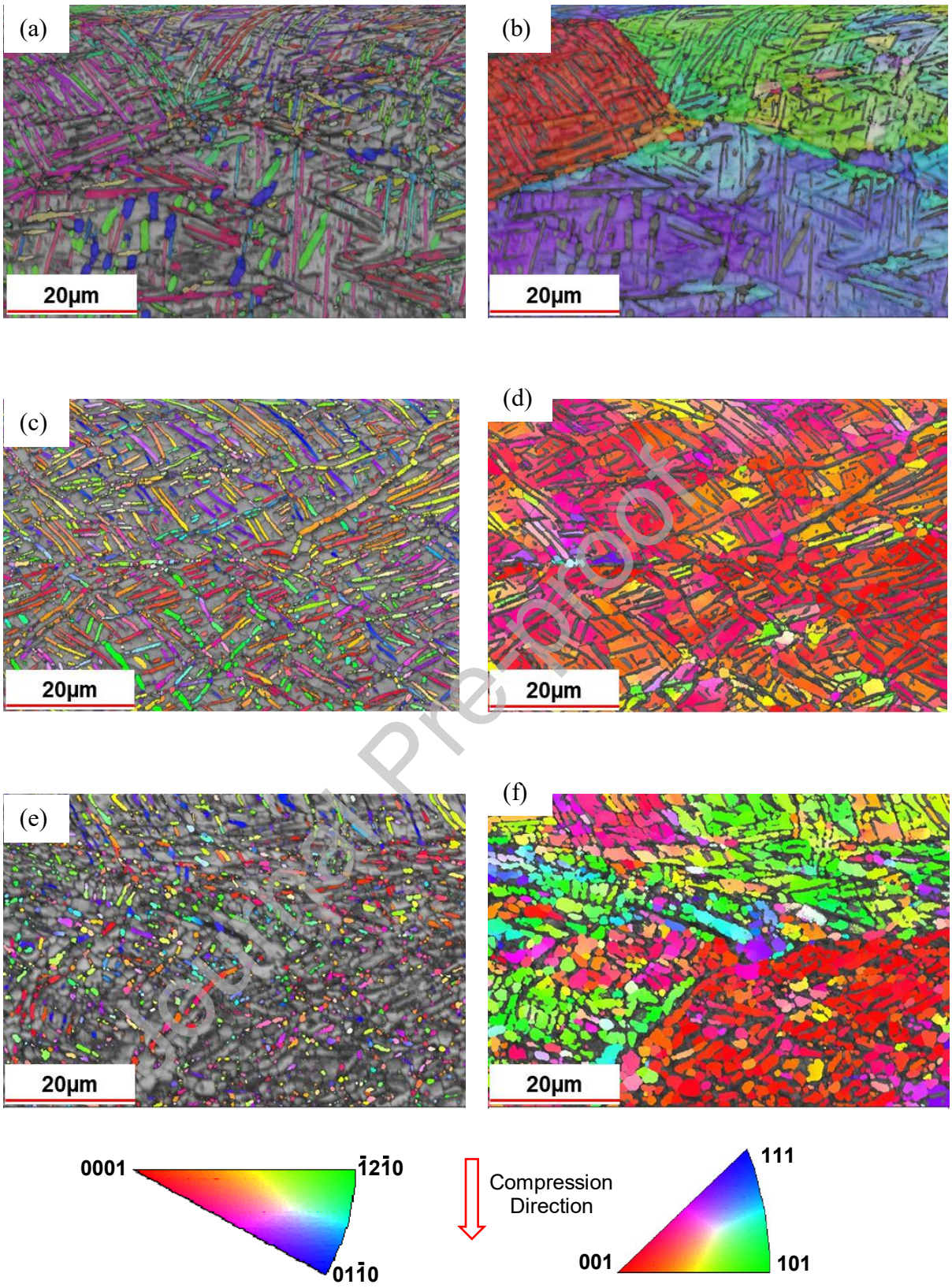

Figure 10: EBSD maps with IPF colouring with respect to the compression direction, superimposed on image quality maps for both α (left) and β (right) phases acquired from the samples subjected to three different levels of reductions, (a) and (b) 30%, (c) and (d) 45%, and (e) and (f) 60%.

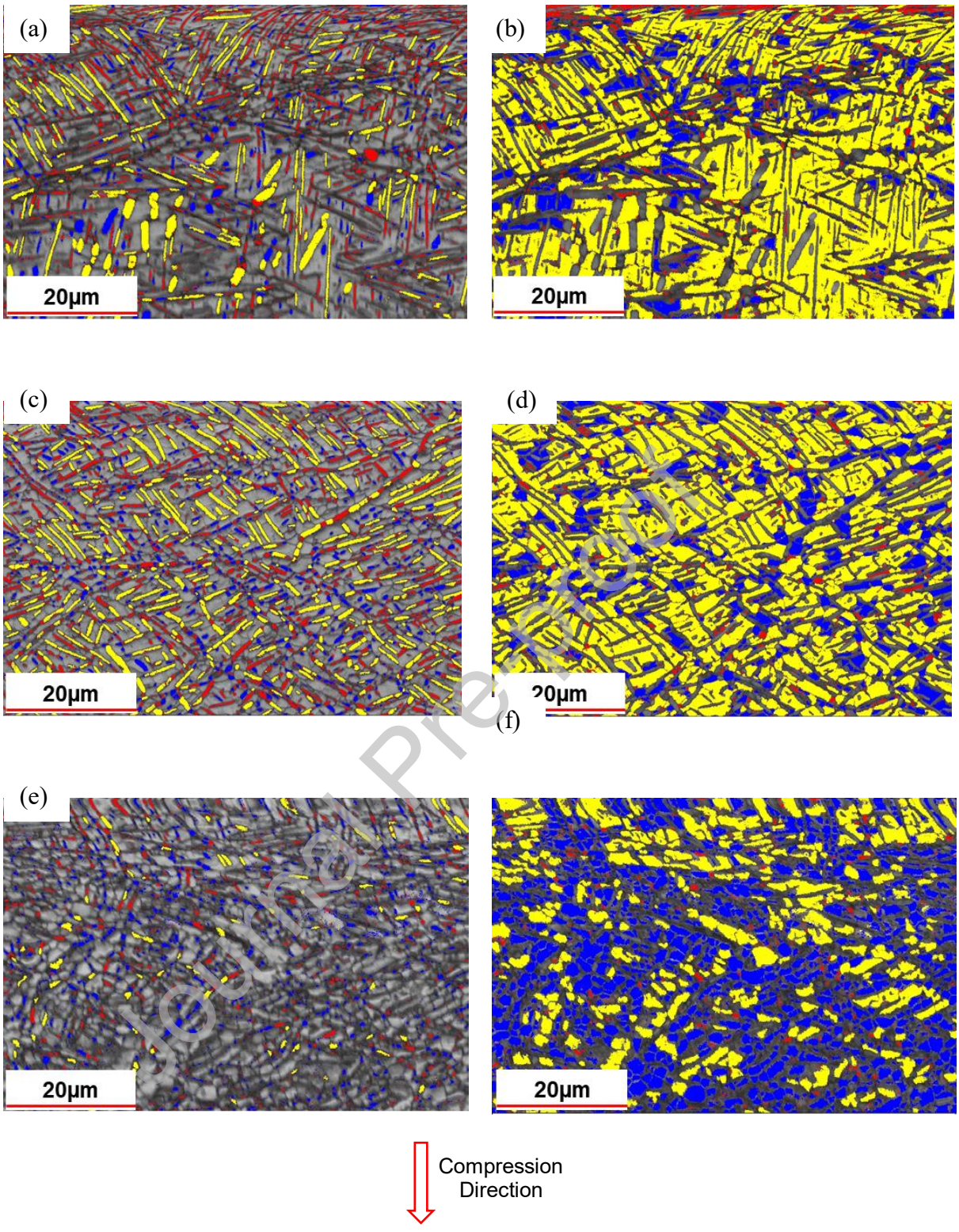

Figure 11: EBSD recrystallisation maps superimposed on image quality maps for both α (left) and β (right) phases obtained from the samples subjected to three different levels of reduction: (a), (b) 30%, (c), (d) 45%, and (e), (f) 60%. The fractions of recrystallised, substructures, and deformed grains are shown in Blue, Yellow and Red, respectively.

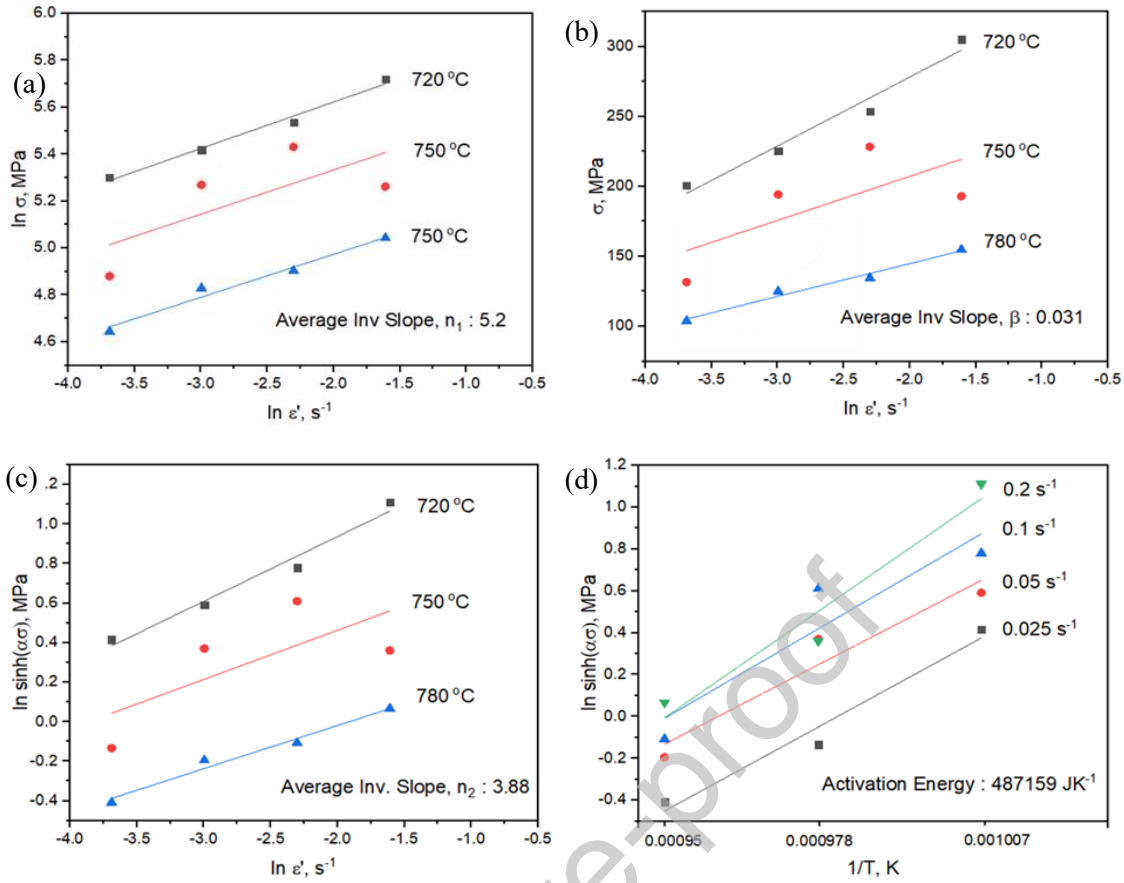

Figure 12: The evaluated relationships between (a) ln(σ) versus ln($\dot{\varepsilon}$), (b) σ versus ln($\dot{\varepsilon}$), (c) ln[sinh(ασ)] versus ln($\dot{\varepsilon}$), and (d) ln[sinh(ασ)] versus 1/T, calculated from the hot compression data measured for the Ti-10V-2Fe-3Al alloy.

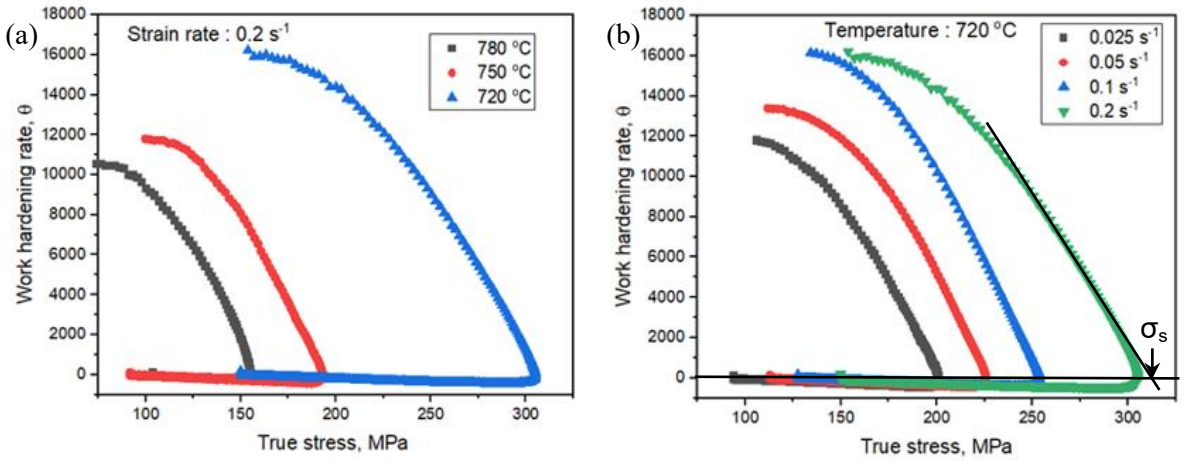

Figure 13: The evaluated relationships between work hardening rate and flow stress (a) under 0.2 s^{-1} strain rate for varying temperatures, and (b) at 720 °C for varying strain rates. σ_s is the saturation stress which was similarly determined for all curves.

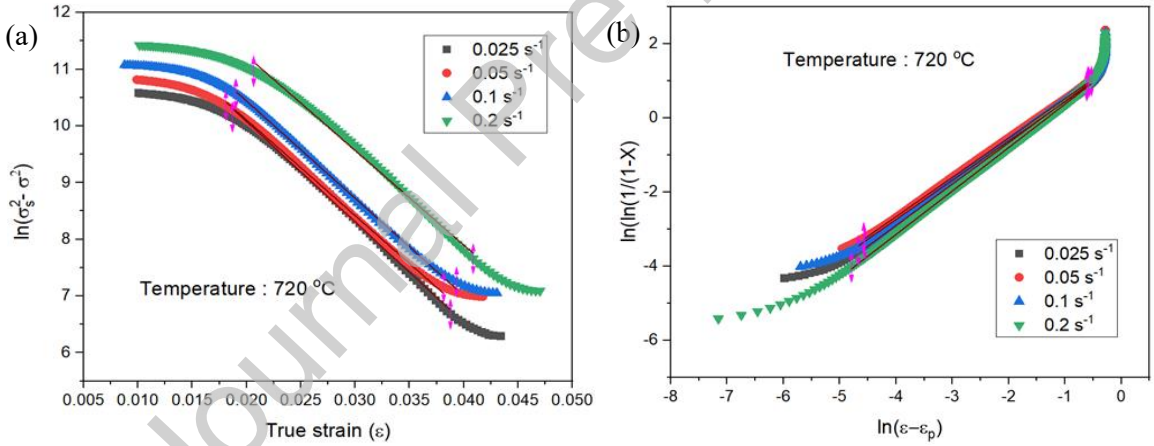

Figure 14: (a) The evaluated relationships between $\ln(\sigma_s^2 - \sigma^2)$ versus true strain at varying strain rates with the plots of best fits to each curve, and (b) the relationships between $\ln(\ln(1/(1-X)))$ and $\ln(\varepsilon-\varepsilon_p)$ at varying strain rates for the tests carried out at the lowest temperature (i.e., 720 °C). In both plots the red lines highlights the best fit to each curve.

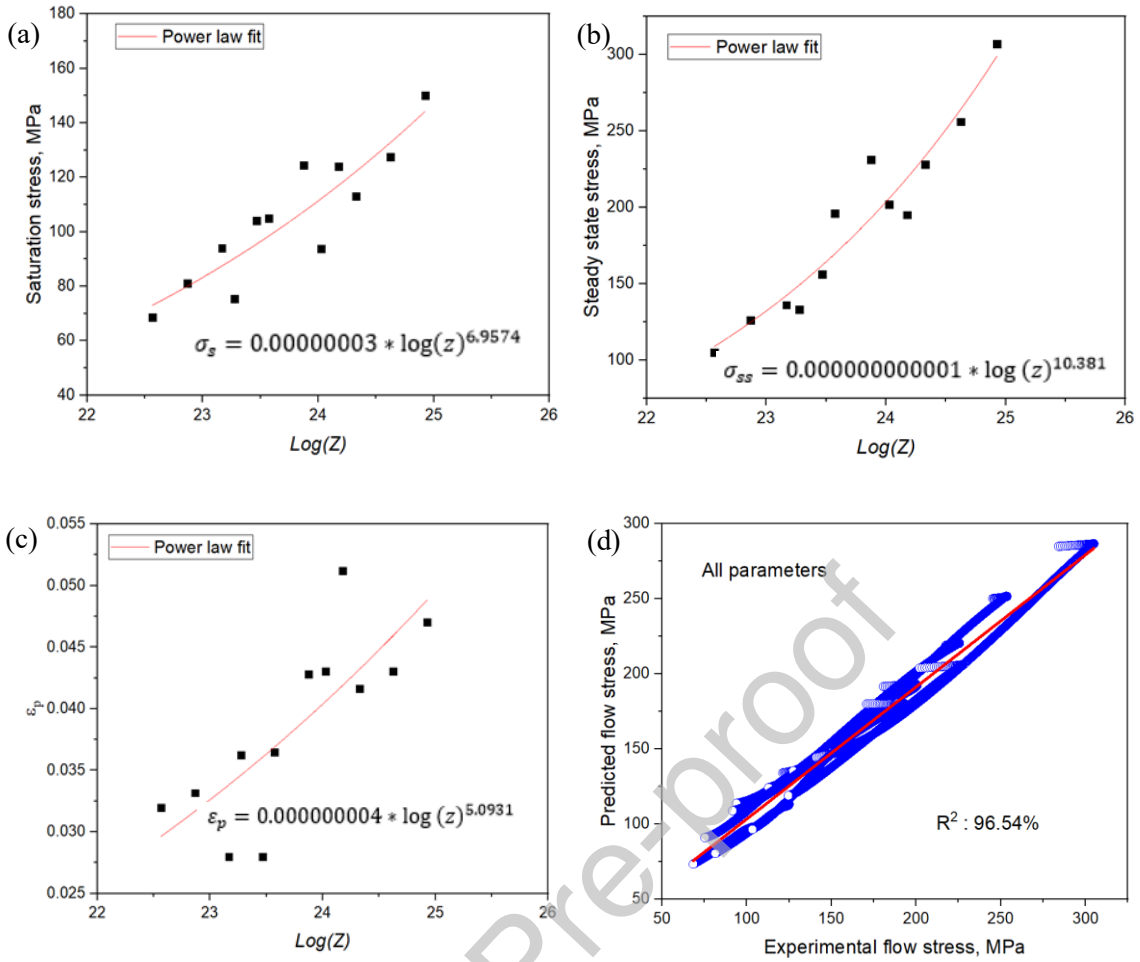

Figure 15: The relationship between *log(Z)* with (a) saturation stress, (b) steady-state stress, and (c) strain equivalent to peak stress (ε_p) and (d) prediction accuracy of the model developed in comparison to the experimental flow stress data for all tests conditions.

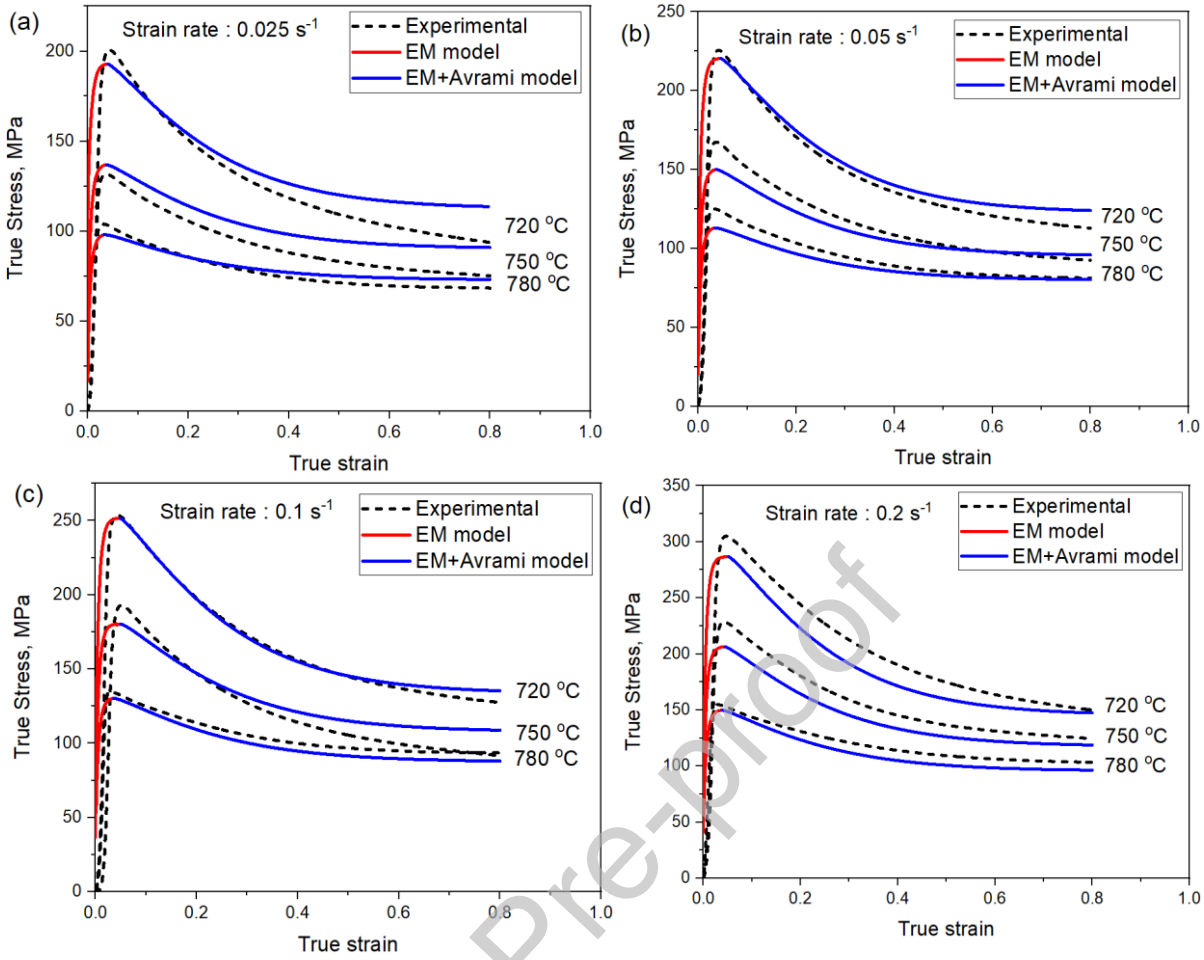

Figure 16: Comparison between the measured and predicted flow curves for the test carried out at different temperatures and under different strain rates, (a) 0.025 s^{-1}, (b) 0.05 s^{-1} , (c) 0.1 s^{-1}, and (d) 0.2 s^{-1}.

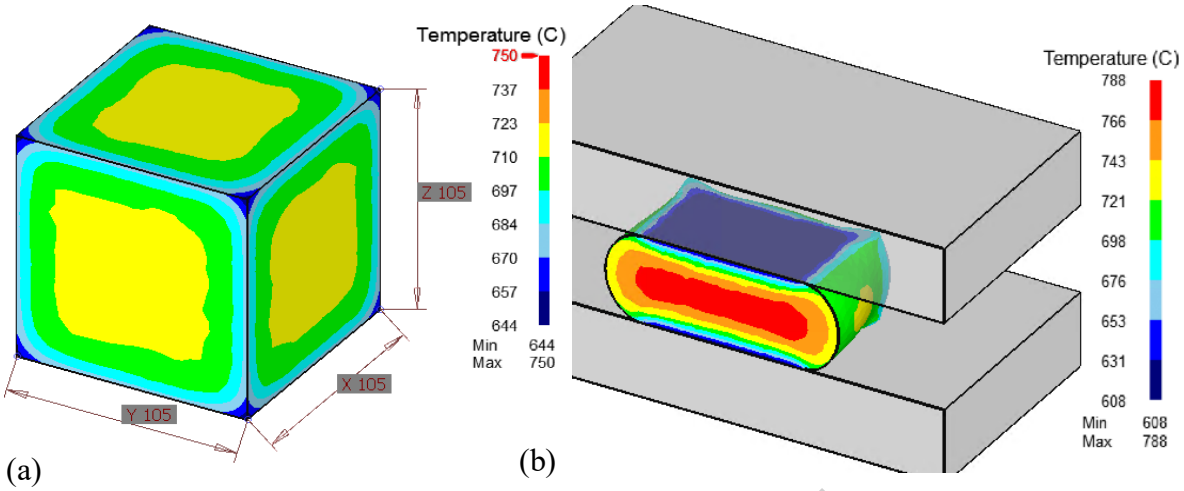

Figure 17: (a) A 3D representation of non-isothermal hot open die forging of the Ti-10V-2Fe-3Al cubic sample, and (b) FE simulation showing temperature distribution in at an intermediate stage during forging process.

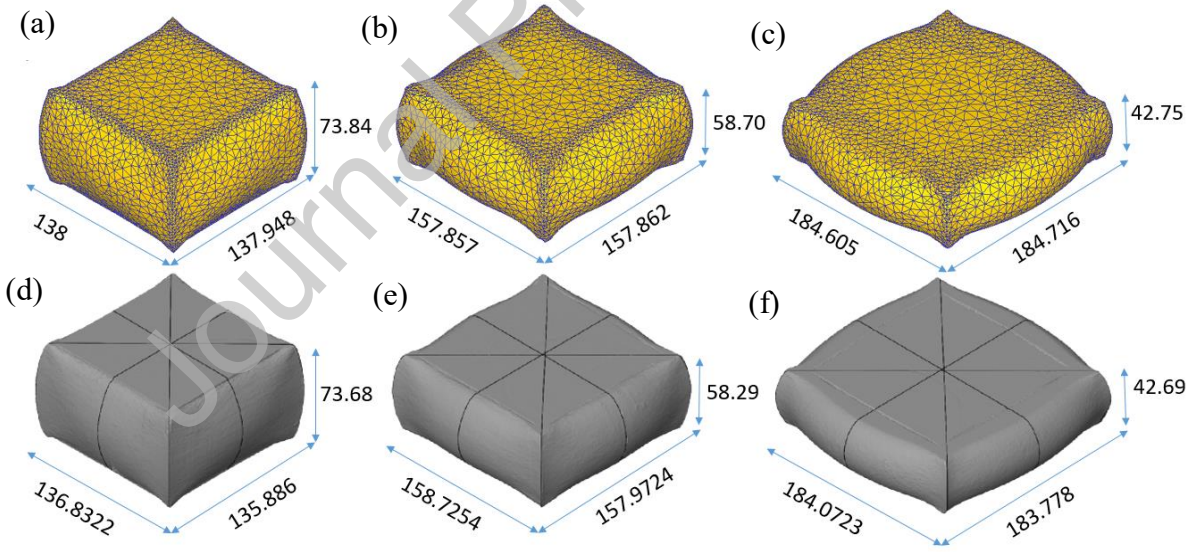

Figure 18: Comparison between the results of FE prediction and experimentally measured shapes and dimensions of the Ti-10V-2Fe-3Al cubes deformed to different levels of reduction: (a) & (d) 30%, (b) & (e) 45% and (c) & (f) 60%. All dimensions are in mm.

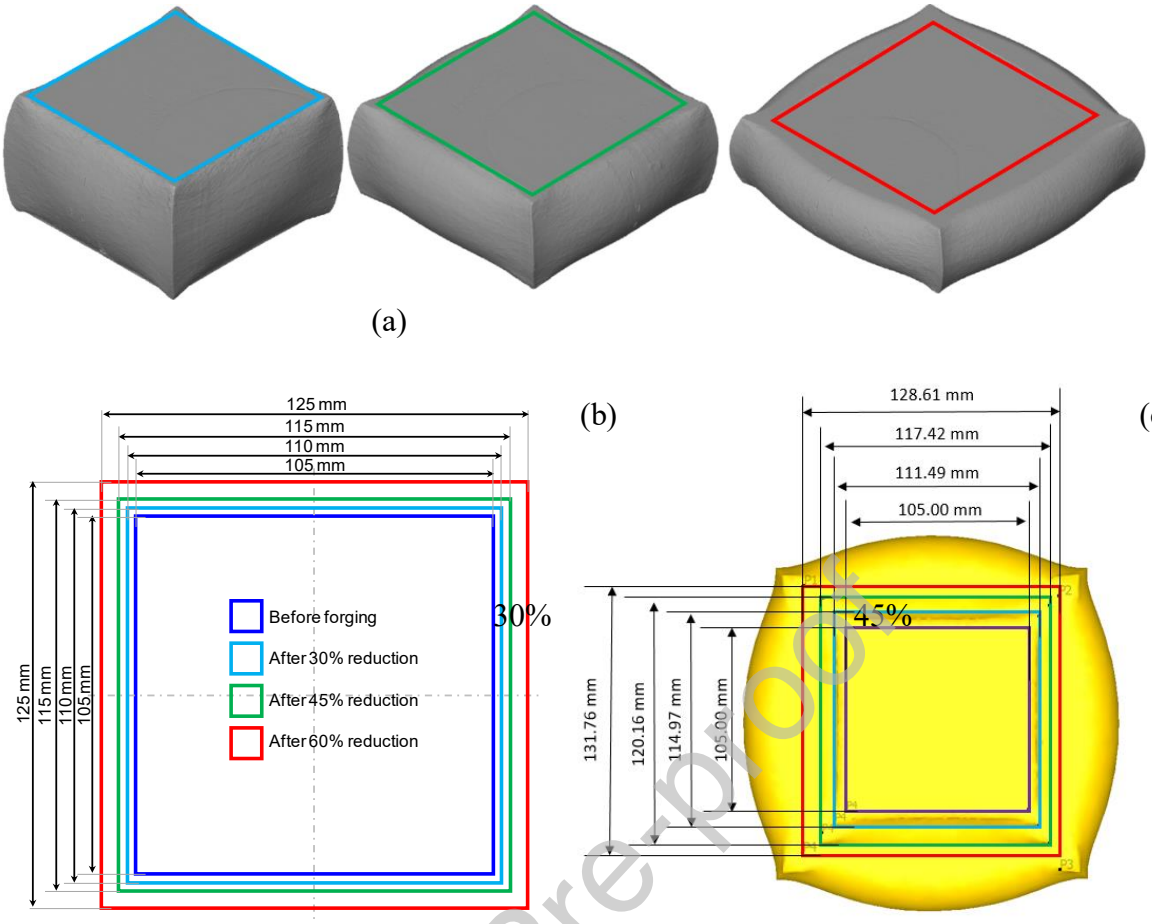

Figure 19: (a) Results of 3D optical scanning showing friction contact regions marked for all cubes forged to different levels of deformation in reduction, (b) Dimensional measurements showing the expansion of friction contact region with increasing the level of reduction, and (c) FE simulated results showing the variation in friction contact regions for different levels of deformation.

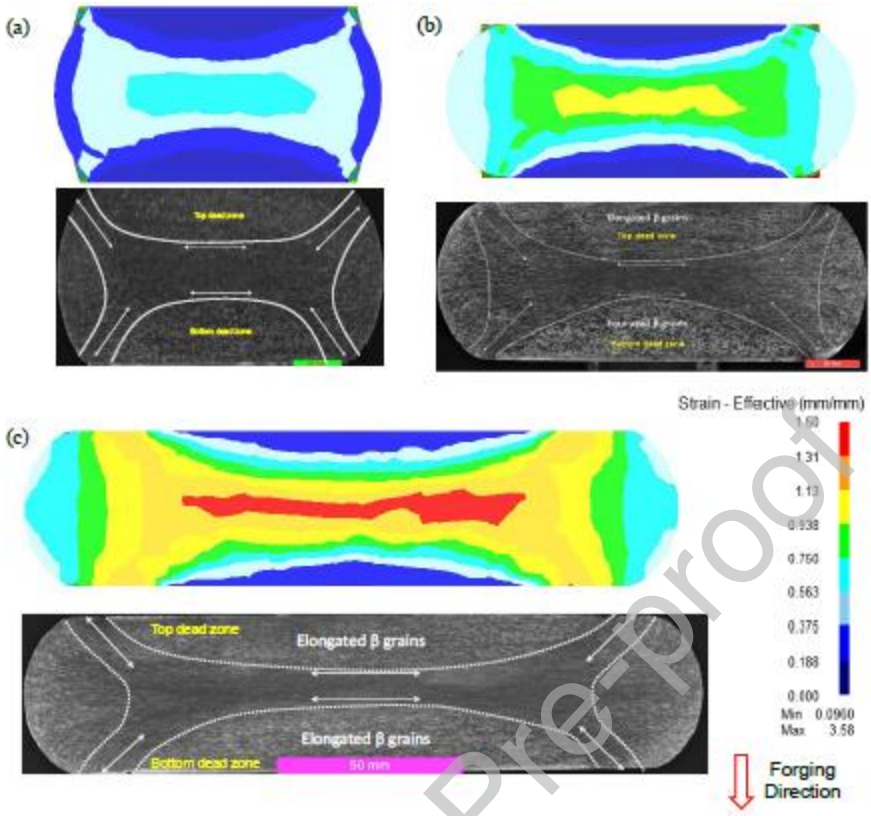

Figure 20: Results of FE simulations and OM appearances of the forged cubes showing the effective strain distribution and grain flow after three different levels of reduction: (a) 30%, (b) 45% and (c) 60%

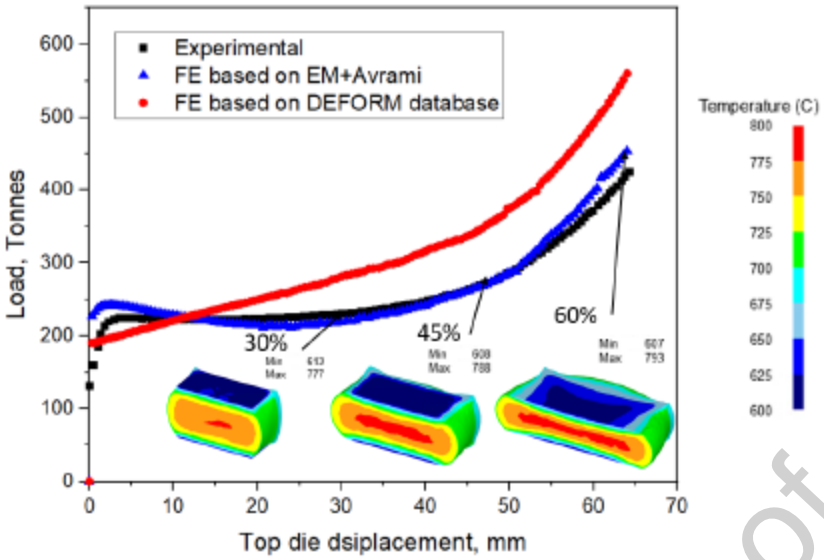

Figure 21: Comparison between the predicted and measured loads plotted against increasing displacement during open die forging of the Ti-10V-2Fe-3Al alloy under a constant speed. Results of FE simulations showing temperature distributions in the billets forged to different levels of reduction are also incorporated.

Table 1. Nominal chemical composition for Ti-10V-2-Fe-3Al alloy

Element	**V**	**Fe**	**Al**	**O**	**N**	**H**	**Ti**
Weight %	10.21	1.87	3.06	≤0.13	≤0.05	≤0.015	Remainder

Table 2: Material constants used for the generalised EM+Avrami model (Equation 14 and 17)

Material Constants	**B**	**a**	**b**	σ_0
Values	70	6	1.2	10*

*MPa.